Comparison of classical beam theory and finite element modelling of timber from fibre orientation data according to knot position and loading type

Guillaume Pot, Robin Duriot, Stéphane Girardon, Joffrey Viguier, Louis Denaud

Comparison of classical beam theory and finite element modelling of timber from fibre orientation data according to knot position and loading type

POT Guillaume [1*], DURIOT Robin [2], GIRARDON Stéphane [1], VIGUIER Joffrey[1], DENAUD Louis [1]

Abstract

Timber mechanical properties assessment relies on grading methods that use non-destructive measurements in input, among which fibre orientation gives satisfactory outcomes. Several models exist in the literature to use fibre orientation data, based on either classical beam theory or finite element modelling. The present paper proposes to compare them for axial and bending loadings. To this end, the main approach was to use several artificial beams, for which fibre orientation was modelled around various knot positions in the tangential plane of wood. It is shown that beam theory modelling, despite considering the heterogeneity of moduli of elasticity in beam longitudinal direction, does not truly represent the actual deformations that can be depicted with finite element modelling. It results in significant differences in the accuracy of the assessment of the local modulus of elasticity, the finite element modelling being better. This finding was supported by experimental results obtained on laminated veneer lumber beams with a high knottiness. Additionally, this paper provides a comparison of different methods to compute localized moduli of elasticity that are typically used as strength predictors. The outcomes indicate that their behaviour depends on the loading type (axial or bending), the knot position in the beam, and the length of the sliding window across which they were computed. A localized bending modulus of elasticity (MoE) computed from the displacements, referred to as the 'apparent MoE', was defined in the objective to improve the accuracy of strength predictions.

Keywords: Grain angle, Laminated Veneer Lumber, Elastic modulus, Strength, Bending, Tensile

Guillaume Pot
*Corresponding author
[1]Arts et Métiers Institute of Technology, LaBoMaP, UBFC, HESAM
Rue Porte de Paris, 71250 Cluny, France
Orcid number: 0000-0001-9751-251X
e-mail: guillaume.pot@ensam.eu

Robin Duriot
[2]Université de Lorraine, LERMAB
27 Rue Philippe Séguin, 88000 Epinal, France
Orcid number: 0000-0002-3811-5861

Stéphane Girardon
[1]Arts et Métiers Institute of Technology, LaBoMaP, UBFC, HESAM
Rue Porte de Paris, 71250 Cluny, France
Orcid number: 0000-0003-2990-6781

Joffrey Viguier
[1]Arts et Métiers Institute of Technology, LaBoMaP, UBFC, HESAM
Rue Porte de Paris, 71250 Cluny, France
Orcid number: 0000-0001-7926-599X

Louis Denaud
[1]Arts et Métiers Institute of Technology, LaBoMaP, UBFC, HESAM
Rue Porte de Paris, 71250 Cluny, France
Orcid number: 0000-0002-4370-6076

1. Introduction

1.1 Modulus of elasticity and strength of timber, under axial and bending loading

The mechanical strength and stiffness of wood material are very variable for many reasons including species, growth conditions, and singularities such as knots, or grain deviation. For this reason, it is important to assess the mechanical properties of any timber product aimed to be used as a structural element. According to European standards, the modulus of elasticity (MoE) and the strength of timber can be measured by either an edgewise bending test or an axial tensile test. Tensile strength is known to be statistically lower than bending strength for structural timber, *i.e.* timber containing knots (Steiger and Arnold 2009; Gil-Moreno et al. 2022). As a result, the characteristic tensile and bending strengths are clearly differentiated in EN 338 (2016) standard.

The reference tensile and bending tests to be used in Europe are described in the EN 408 (2012) European standard. According to this standard, specimen's length should exceed the test span so they can be placed such as their weakest area, typically where highest knotiness is located, is in the middle of the span. In either of these tests, a so-called "local MoE" is obtained by a device placed in the central area of the specimen, measuring the displacement of the specimen over a distance of five times the depth of the specimen (depth being the larger dimension of the rectangular cross-section). This induces that the local MoE measured according to the European Standards is the weakest local MoE of the specimen, as the MoE is actually variable along the length. The strength properties are determined from the same tests if the failure effectively occurs away from the grips in the tensile test and within the maximum bending moment area in the bending test.

Timber exhibits the particular behaviour that the strength of the tested specimens is well correlated to their MoE, as it has been shown in large-scale studies (Hanhijärvi and Ranta-Maunus 2008; Drewett 2015; Viguier 2015; Olsson and Oscarsson 2017; Rais et al. 2021). As a result, when dealing with structural timber containing knots, both the local MoE and the strength mainly rely on the stiffness around the weakest area of the board. For this reason, it is crucial to assess the effect of wood heterogeneities such as knots and grain deviations on the stiffness located in the weakest area of the board. This strategy was followed in the modelling method proposed by various authors (Olsson et al. 2013, Hu et al. 2018, Viguier et al. 2018, Lukacevic et al. 2019, Briggert et al. 2020, Duriot et al. 2021b, Huber et al. 2022).

1.2 Fibre orientation data sources

To determine the heterogeneity of the MoE of a wooden beam, it is possible to rely on grading machines that measure locally a physical parameter of the wood material, like local fibre orientation or local density. Indeed, wood being a highly anisotropic material, strength and elastic properties are far better in the longitudinal direction of fibre than in the perpendicular directions, thus fibre orientation is a parameter of first importance. Fibre orientation can be measured by using the so-called "tracheid effect", which is based on the anisotropic scattering of concentrated laser light projected to wood surface (Simonaho et al. 2003; Nyström 2003). This technology is implemented in current industrial scanners which use rows of laser dots to obtain a typical resolution of about a couple of millimeters in the direction of convey and 4 mm crosswise (Olsson et al. 2013; Longuetaud et al. 2022).

Wood fibre orientation around knots can also be estimated from the so-called "flow-grain" analogy (Goodman and Bodig, 1980). This method assimilates the grain deviations in the vicinity of a knot to the streamlines of a laminar fluid flow around the knots which are supposed to be elliptical or cylindrical objects. Foley (2001) used the flow-grain analogy, more precisely the Rankine oval method, to model how the fibres deviate around a knot in a given growth layer, *i.e.* in the longitudinal-tangential LT-plane of the tree, also called tangential plane. Indeed, wood is formed in a tree by longitudinal and radial growth, thus it can be seen as an orthotropic material in a cylindrical coordinate system. To model fibre orientation in the longitudinal-radial LR-plane of the knot axis, this author used exponential functions. Frayssinhes et al. (2020) applied the flow-grain analogy on veneer sheets obtained by rotary peeling. Such veneers are thin (typically 3 mm) sheets of wood, that are in the LT orthotropic plane of the tree due

to the processing. These authors compared the modelling by Rankine oval method of fibre deviation around the knots in LT-plane with laser-dot measurements on a total of 289 knots of various diameters. The modelled fibre deviation around knots revealed to be qualitatively in agreement with the experimental measurements. This fibre deviation modelling was, however, not perfect: the root mean square error topped 18° very close to the knot edge, decreasing to less than 10° at a distance of 3 knot radius from the knot center.

From these different sources of fibre orientation data, different authors proposed empirical, analytical or finite element (FE) models to estimate timber MoE and strength.

1.3 Classical composite beam theory applied to fibre orientation data

A representative elementary volume of clear wood can be considered as an orthotropic material in a LTR-coordinate system where L is the longitudinal direction of the fibres, T the tangential direction, and R is the radial direction. Assuming linear elasticity, the corresponding compliance matrix is:

$$\begin{bmatrix} \frac{1}{E_L} & -\frac{\nu_{TL}}{E_T} & -\frac{\nu_{RL}}{E_R} & 0 & 0 & 0 \\ -\frac{\nu_{LT}}{E_L} & \frac{1}{E_T} & -\frac{\nu_{RT}}{E_R} & 0 & 0 & 0 \\ -\frac{\nu_{LR}}{E_L} & -\frac{\nu_{TR}}{E_T} & \frac{1}{E_R} & 0 & 0 & 0 \\ 0 & 0 & 0 & \frac{1}{G_{LT}} & 0 & 0 \\ 0 & 0 & 0 & 0 & \frac{1}{G_{LR}} & 0 \\ 0 & 0 & 0 & 0 & 0 & \frac{1}{G_{RT}} \end{bmatrix} \quad (1)$$

with E_L, E_T and E_R the MoEs in the longitudinal, tangential and radial direction of the fibre, respectively, G_{LT}, G_{LR}, and G_{RT} the shear moduli in LT, LR, and RT orthogonal planes, respectively, ν_{LT}, ν_{TL}, ν_{LR}, ν_{RL}, ν_{RT} and ν_{TR} the Poisson's ratio according to the corresponding different directions.

Although this is the constitutive law that is the closest to the actual material, it is inconvenient to make a practical difference between T- and R-directions. As a result, practical modelling of timber usually considers a transverse isotropic behaviour, in which tangential and radial properties are the same. Assuming a plane stress state, Equation (1) can be summarized as Equation (2):

$$[\mathrm{S}] = \begin{bmatrix} \frac{1}{E_L} & -\frac{\nu_{TL}}{E_T} & 0 \\ -\frac{\nu_{LT}}{E_L} & \frac{1}{E_T} & 0 \\ 0 & 0 & \frac{1}{G_{LT}} \end{bmatrix} \quad (2)$$

Olsson et al. (2013) proposed to use the fibre angles measured by laser dot scanning, to compute for every data point of sawn board surfaces E_x, the MoE in the main, lengthwise x-direction of the specimen, as the inverse of the first component of the compliance matrix $[\mathrm{S}']$ obtained by transformation, more specifically a rotation of the coordinate system, of the compliance matrix in the material principal direction $[\mathrm{S}]$, which gives:

$$[\mathrm{S}'] = [T_\theta^{-1}]\,[S]\,[T_\theta] = \begin{bmatrix} \mathrm{S}'_{xxxx} & \mathrm{S}'_{xxyy} & \mathrm{S}'_{xxxy} \\ \mathrm{S}'_{xxyy} & \mathrm{S}'_{yyyy} & \mathrm{S}'_{yyxy} \\ \mathrm{S}'_{xxxy} & \mathrm{S}'_{yyxy} & \mathrm{S}'_{xyxy} \end{bmatrix} \quad (3)$$

$$E_x = \frac{1}{S'_{xxxx}} = \frac{1}{\frac{1}{E_T}\sin^4(\theta) + \frac{1}{E_L}cos^4(\theta) + \left(\frac{1}{G_{TL}} - 2\frac{\nu_{LT}}{E_L}\right)\sin^2(\theta)\,cos^2(\theta)} \quad (4)$$

where θ is the angle between the projected fibre direction in the plane of the considered surface and specimen main x-direction (which was measured by laser dot scanning in the present case), T_θ is the transfer matrix, from the local fibre LT coordinate system to the global specimen coordinate system, dependent on θ, and E_x is a MoE computed locally at the considered data point position, *i.e.* at the surface of the board since it is where the laser dot measurement was performed.

Olsson et al. (2013) proposed a method to attribute MoE values within the volume of the board from the E_x computed at board surfaces, which gives $E_x(x, y, z)$, the lengthwise MoE for each x (lengthwise), y (depth-wise) and z (thickness-wise) positions in a beam. These authors proposed to use this MoE in an analytical modelling, considering composite beam theory where the map of $E_x(x, y, z)$ is the MoE of a heterogeneous, but isotropic beam. Assuming classical Euler-Bernoulli beam theory (BT) hypothesis, *i.e.* displacements and strains remain small, plane cross-sections initially normal to the beam's axis remain plane, normal to the beam axis, and undistorted, $E_x(x, y, z)$ can be integrated over each cross-section along the beam, to compute an edgewise bending MoE $E_{b,BT}(x)$ at each x lengthwise position:

$$\mathrm{E}_{b,BT}(x) = \frac{\iint E_x(x, y, z)\left(y - \overline{y(x)}\right)^2 dydz}{I} \quad (5)$$

where I is the quadratic moment of area of a rectangular beam, equals to $th^3/12$ with t the thickness and h the depth of the beam, $\overline{y(x)}$ is the y position of the neutral fibre across the depth of the heterogeneous beam at the lengthwise position x.

As reported in Briggert et al. (2020), the same analytical method can be applied to obtain $E_{a,BT}(x)$, the MoE under homogeneous tensile or compressive (*i.e.* axial) stresses integrated at each x lengthwise position of the composite beam:

$$E_{a,BT}(x) = \frac{\iint E_x(x, y, z)\, dydz}{th} \quad (6)$$

$E_{a,BT}(x)$ or $\mathrm{E}_{b,BT}(x)$ are MoE profiles with a high lengthwise resolution of 1 mm between data point or less, corresponding to the lengthwise scanning resolution of dot laser scanning.

Oscarsson et al. (2014) proposed to apply a moving average to smooth these MoE profiles across a given sliding window length to obtain the averaged localized MoE under axial or bending loading. They showed that the minimum localized MoE found along each board was better correlated to the specimen's strength if the length of the sliding window was 90 mm for boards with a depth of 145 mm subjected to bending loading, and 25 mm for boards with a depth of 56 mm subjected to tensile loading. In the following studies of the same team using the same method (Olsson and Oscarsson 2017; Olsson et al. 2018; Briggert et al. 2020), a constant sliding window length of 90 mm was applied for various species, cross-sections and loading type.

It should be noted that Equation (4) can be very well approximated by Hankinson empirical formula (Equation (7), Hankinson 1921), if an adequate n parameter is used.

$$E_{x,Hank} = \frac{1}{\frac{1}{E_\mathrm{T}}\sin^n(\theta) + \frac{1}{E_\mathrm{L}}cos^n(\theta)} \quad (7)$$

This well-known formula in wood science expresses the non-linear decrease of the MoE of wood material when being angled from fibre principal direction. It has been used instead of Equation (4) in several models (Viguier et al. 2017; Viguier et al. 2018; Duriot et al. 2021b; 2021a; Ehrhart et al. 2022). Viguier et al. (2018) and Duriot et al. (2021a, b) proposed analytical models based on BT as well as that of Olsson et al. (2013), but applied on veneer-based products. Indeed, veneers can be glued together to make for example laminated veneer lumber (LVL). Both Viguier et al. (2018) and Duriot et al. (2021b) used fibre orientation measured by laser dot scanning of the veneers to model the MoE in bending of 41 and 10 LVL beams, respectively.

1.4 Finite element modelling applied to fibre orientation data

Hu et al. (2018) proposed a method to interpolate fibre orientation measured at sawn board surfaces to use these angles in a 3D FE model. In this model, each element has potentially a different angle with board main direction. This angle is used in the FE model implying that each element gets a local material compliance matrix $[S']$ as in Equation (3), but on contrary to BT modelling, the full compliance matrix is used and thus the anisotropic behaviour is taken into account in the FE modelling. These authors used the obtained strain field to estimate the localized bending MoE according to the lengthwise position in the beam by performing a linear regression of the lengthwise strains ε_{xx} along y-direction for each x position. This gives $\widehat{\varepsilon_{xx}}(x,y)$, the linear approximated longitudinal strain. In BT, for a homogeneous beam, ε_{xx} is perfectly linear and its slope over beam depth (y-direction) is inversely proportional to the MoE. Hu et al. (2018) assumed that the approximated $\widehat{\varepsilon_{xx}}(x,y)$ is related to the edgewise bending MoE at each x position, denoted in the present paper $E_{b,\varepsilon,FE}$, and computed as:

$$E_{b,\varepsilon,FE}(x) = \frac{M}{I\frac{\partial\overline{\widehat{\varepsilon_{xx}}(x)}}{\partial y}} \tag{8}$$

where M is the applied bending moment.

Hu et al. (2018) compared FE model results to that of the BT model of Olsson et al. (2013) and also digital image correlation (DIC) observations on two boards of Norway spruce. These authors found that FE model was able to capture better the actual compliance of the boards.

The criterion of Hu et al. (2018), has been used by other authors (Lukacevic et al. 2019; Huber et al. 2022) to estimate the MoE profiles along boards length. Lukacevic et al. (2019) also used a 3D FE model, but they used Foley's method (Foley 2001) to obtain the fibre orientation in 3D from knot measurements. Huber et al. (2022) also proposed a 3D FE model by modelling fibre orientation around knot shapes obtained from X-Ray computer tomography, on 20 Norway spruce boards of 50 × 100 mm² cross-section. They observed that the mimimum localized MoE $E_{b,BT}$ computed with the BT analytical method as in Equation (6) and smoothed with a 60 mm Gaussian window, gave a better correlation with strength than $E_{b,\varepsilon,FE}$ computed with the method of Hu et al. (2018) with sliding window lengths ranging from 0 to 100 mm. On the contrary, Olsson et al. (2022) compared these same two methods on a dataset of 241 Douglas fir boards of 40 × 100 mm² cross-section, and consistently found better correlations with either bending strength or experimental local MoE by using FE method.

Another natural way to get a strength predictor when dealing with FE results is to compute a failure criterion based on the stresses such as a Tsaï-Hill criterion. This approach has been studied by several authors (Baño et al. 2011; Grazide et al. 2018; Saad and Lengyel 2022), of which the first two proposed a very similar approach as the present work, studying artificial beams with different knot positions (but without comparison with classical BT modelling). As explained by Grazide et al. (2018), an equivalent strength according to Tsaï-Hill criterion can be obtained as follows for a beam modelled in two dimensions and subjected to tensile or bending stresses:

$$f_{eq}(x,y) = \frac{\sigma}{\sqrt{\left[\left(\frac{\sigma_{LL}(x,y)}{f_{t,L}}\right)^2 + \left(\frac{\sigma_{TT}(x,y)}{f_{t,T}}\right)^2 + \left(\frac{\tau_{LT}(x,y)}{f_v}\right)^2\right]}} \tag{9}$$

where σ_{LL} is the stress in the L direction of the fibre, $f_{t,L}$ is the corresponding tensile strength in the L direction of the fibre; σ_{TT} is the stress in the T direction of the fibre, $f_{t,T}$ is the corresponding tensile strength in the T direction of the fibre; τ_{LT} is the shear stress in LT plane of the fibre, f_v is the corresponding shear strength in LT plane; σ is the maximum normal (*i.e.* axial) stress due to tension or bending loading.

1.5 Scope and objectives

According to the few references of the literature which make the comparison, FE modeling derived from fibre orientation data generally appears to be more representative of wood mechanical behaviour than BT modeling, in particular in knotty areas with large fibre deviations. This seems consistent since FE modelling allows the complexity of the phenomena occurring in such a heterogeneous area to be taken into account. However, analytical models remain interesting because they can be computed in a very short amount of time, which is advantageous in the context of wood quality assessment by machines at industrial speeds. It is therefore useful to understand the reasons for the differences in modelled localized MoEs between FE and BT mechanical modelling and to quantify them. The available literature is very sparse about such comparisons.

The localization of MoE variations around knots poses challenges in accurately predicting the material's performance, particularly under different loading conditions. Understanding the nuanced relationship between knot position, localized MoE, and modeling approaches is critical in enhancing predictive accuracy for structural applications. To this end, the present work aims to compare the local MoE as defined in EN 408 (2012), the localized MoE and the strength predictors that are obtained by FE and BT mechanical modelling under axial and pure bending loading for several artificial beams for which fibre orientation was modelled in 2D in the longitudinal-tangential plane for various knot positions. To have an experimental validation of the results, it is also proposed to compare the local MoEs obtained by these models to that of actual LVL beams tested in edgewise bending. By using this material and direction of loading, the timber was indeed loaded in the longitudinal-tangential plane as for artificial beams.

The overall objective is to provide researchers and engineers that are interested in the mechanical behaviour of structural timber containing knots with a better understanding of the respective functioning and limitations of FE and BT modelling and the strength predictors extracted from it. In more detail, we propose in this study to: (1) investigate variations in localized MoE along timber beams with knots under axial tension and pure bending; (2) assess the influence of knot position on mechanical behaviours, emphasizing disparities between axial and bending loading scenarios; (3) compare and contrast different strength predictors obtained from FE and BT modelling;

2. Materials and method

2.1 Lists of main symbols used in the article

Table 1 lists the main abbreviations and the main parameters that were used, while Table 2 lists the output variables that are discussed in this paper.

Symbol / Abbreviation	Description
MoE	Modulus of elasticity
Local MoE	Term used in EN 408 (2012) to refer to the MoE computed from the deformation of a specimen over a distance of five times the depth of the rectangular cross-section when it is subjected to tension or bending
Localized MoE	MoE computed from a mechanical model to represent the MoE over a short span, known as the "sliding window length", along the entire length of the board, to create a MoE profile from which the minimum value is usually used as a strength predictor
BT	Analytical method to compute the displacements of a beam subjected to axial or bending loading, based on composite beam theory and Euler-Bernoulli beam theory
FE	Numerical, finite element method to compute the displacements of a beam subjected to axial or bending loading
E_L	MoE in the longitudinal direction of fibres (GPa)
E_T	MoE in tangential direction of fibres (GPa)
G_{LT}	Shear modulus in tangential-longitudinal plane of fibres (GPa)
ν_{LT}	Poisson's ratio characterizing tangential strains in relation to longitudinal strains
δ	Sliding window length across which localized MoE was computed
x	Coordinate in lengthwise direction of the beam (mm)
y	Coordinate in crosswise direction (depth) of the beam (mm)
h	Depth of the beam (mm)
L	Length of the beam (mm)
t	Thickness of the beam (mm)
y_k	Knot position in y-direction
$\theta(x,y)$	Angle between the fibre direction and specimen main direction $\vec{x}$ in the plane of the considered surface, at coordinates (x,y) (°) (see Fig.3)
$E_x(x,y)$	Localized MoE projected to $\vec{x}$ axis at coordinates (x,y) (GPa) (z dimension not needed in the present work dealing with 2D modelling only)

Table 1. List of main parameters used and abbreviations

			Axial loading (Equation number)	Bending loading (Equation number)	Line style in figures	Main reference in literature
Beam theory (BT) modelling	Localized MoEs	Averaged MoE	$E_{a,avg,\delta,BT}$ (15)	$E_{b,avg,\delta,BT}$ (21)	·····	Olsson et al. (2013)
		Apparent MoE	$E_{a,app,\delta,BT}$ (16)	$E_{b,app,\delta,BT}$ (22)	------	Present paper
	Local MoE		$E_{a,l,BT}$ (18)	$E_{b,l,BT}$ (23 + 24)	------	EN 408 (2012)
Finite element (FE) modelling	Localized MoEs	MoE from strains	$E_{a,\varepsilon,\delta,FE}$ (28)	$E_{b,\varepsilon,\delta,FE}$ (32)	–·–·–·	Hu et al. (2018)
		Apparent MoE	$E_{a,app,\delta,FE}$ (27)	$E_{b,app,\delta,FE}$ (31)	——	Present paper
	Local MoE		$E_{a,l,FE}$ (29)	$E_{b,l,FE}$ (23 + 33 or 34)	——	EN 408 (2012)
	Tsaï-Hill criterion		$f_{t,eq}$ (9)	$f_{b,eq}$ (9)	–··–··–··	Grazide et al. (2018)
Experimental LVL	Local MoE		Not tested	$E_{b,l,exp}$ (23)	NA	EN 408 (2012)

Table 2. List of main variables that are discussed in this paper along with their origin and line style in figures.

2.2 Material and fibre orientation data as modelling input

2.2.1 Artificial timber beams

Artificial timber beams in LT plane were generated with different knot positions according to the method of Foley (2001), in a similar way to what Frayssinhes *et al.* (2020) did. A function drives the flow, between an inlet (source) and an outlet (sink), and how elliptical obstacles are bypassed. The flow lines generated are then assimilated to the wood fibres, whose local angle can be determined (Foley, 2001).

Modelled knots had a circular shape. The knot diameter of 72.5 mm (half of the beams' depth) was chosen to highlight knot influence. Such large knots are frequent for Douglas Fir grown in France, even if being more to the end of the spectrum. Flow function parameters are those determined for Douglas fir by Frayssinhes et al. (2020). These Douglas-fir parameters were applied by coherence with the experimental LVL material.

Five artifical beams were modelled as shown in Fig. 1. Their dimensions were L = 2710 mm × h = 145 mm × t = 3 mm. These dimensions were chosen in accordance with that of the experimental LVL beams described in the next section. It may be noticed that thickness had no importance for the artificial beams which were modelled in two dimensions. The generated angle grid had a resolution of 1 mm × 1 mm.

The first artificial beam, shown in Fig. 1a, is a homogeneous beam with zero fibre angle at any point of the beam. Fig. 1e shows a beam with a circular knot of diameter D = 72.5 mm for which the center coordinates are ($x_k = \frac{L}{2}$; y_k = 0). An area of fibre orientation deviation around the knot induces variations of $\theta(x, y)$ values according to a « butterfly » shape. The beams shown in Fig. 1d, Fig. 1c, and Fig. 1b follow the same principle, with the exception that the centre of the knot is successively translated from the $\vec{y}$ axis by $-\frac{h}{4}$ according to the beam of Fig. 1e. This gives the position of the centre of the knot at the coordinates ($x_k = \frac{L}{2}$; $y_k = -\frac{h}{4}$), ($x_k = \frac{L}{2}$; $y_k = -\frac{h}{2}$), ($x_k = \frac{L}{2}$; $y_k = -\frac{3h}{4}$), respectively.

	Local fibre orientation $\theta(x, y)$ beam colormap	**Knot center position (x_k, y_k)**	**Marker color**

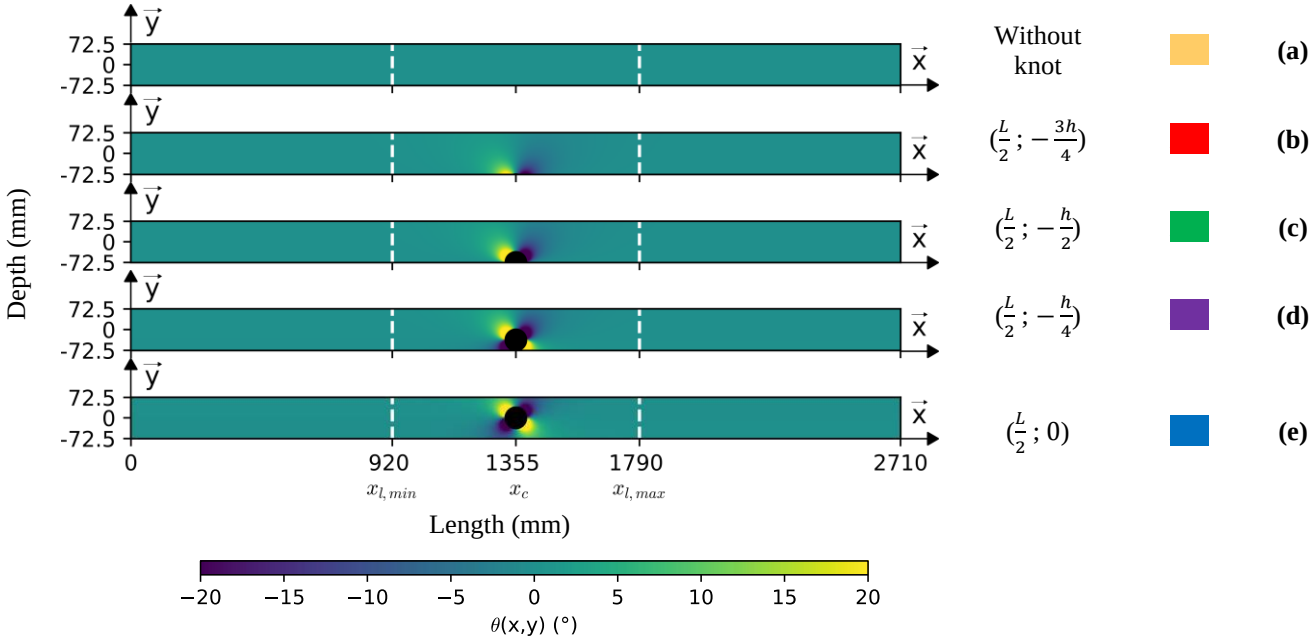

Fig. 1. Modelled artifical beams: (a) homogenous beam, (b) (c) (d) (e) beams with a single knot with indicated centre coordinates. Colours represent angle value, the knot being black since fiber angles in the knot are not modelled (considered as isotropic).

2.2.2 Experimental LVL beams

The experimental material comes directly from Duriot et al. (2021a,b). In Duriot et al. (2021a), Douglas-fir logs that were grown in Burgundy region of France were peeled in 3 mm-thick veneers. They were scanned by a laser-dot instrument exploiting the tracheid effect at the resolution of 16 mm in the longitudinal direction and 3.5 mm in the tangential direction of wood fibres. A grid of the local fibre orientation $\theta(x, y)$ was linearly interpolated from the laser-dot measurements for each of the veneers. This interpolation resulted in a fiber angle dataset with a resolution of 1 mm × 1 mm, which was used as input for LVL beam modelling. In Duriot at al. (2021b), batches of 60 veneers with equivalent density and grain angle distributions were made. Two LVL panels of $n_p = 15$ plies were manufactured from it, with final dimensions of about 2800 mm × 850 mm × 45 mm. Five beams were cut in each panel, the nominal dimensions of each beam were 2710 mm × 145 mm × 45 mm (Fig. 2a).Veneers position were arranged first in a favourable configuration for bending, which consisted in placing the higher grade veneers (higher density, lower fibre orientation variation) at the centre of the panel in the LVL lengthwise direction and the lower grade veneers at the ends (an example of the resulting beam MoE map is shown in Fig. 2b). An unfavourable configuration was also tested, reversing the previous strategy (example Fig.2c). This strategy aims to exaggerate the so it could make clearer the differences between the modelling methods. The beams were tested in a four-point edgewise bending test configuration and the experimental local modulus of elasticity was measured, following EN 408 (2012) standard.

2.3 Material properties

In this study, FE and BT modelling were applied to both multi-plies LVL experimental beams and monolithic artificial timber beams. For LVL, beams were made of several veneers. These veneers are associated with index v (Fig. 2a). Several of them make up each ply of the material, associated with index p, as shown in Fig. 2a. In order to summarize the following explanations and equations, the artificial timber beams can be considered as a one-ply "LVL" composed of one veneer ($v = 1, p = 1$).

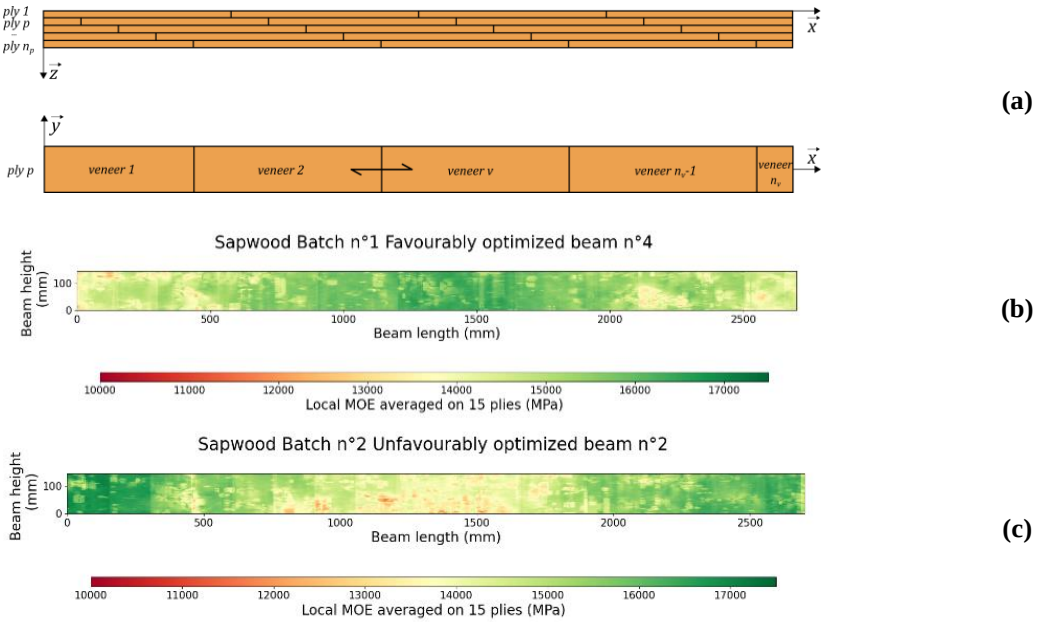

Fig. 2. (a) Schematical representation of the constitution of a LVL beam made of several plies (p index) and veneers (v index) (arrow represents main grain direction), (b) example of the modeled MoE repartition of a favourably optimized beam, borrowed from Duriot et al. (2021b), (c) example of the modeled MoE repartition of an unfavourably optimized beam, borrowed from Duriot et al. (2021b)

2.3.1 Orthotropic elastic properties of clear wood

"Clear wood", or more precisely fibres material properties were defined by the compliance matrix $[S_{v,p}]$ in the material LT-system as in Equation (2) for each veneer and ply. E_L, the MoE in longitudinal direction of fibres, was calculated as in Duriot al. (2021b) by taking into account the overall density of the veneer at 12% moisture content in kg.m^{-3}, $\overline{\rho_{v,p}}$, using a linear equation from Pollet et al. (2017), or a value of 16.8 GPa for artificial beams:

$$E_L = \begin{cases} 0.036605\,\overline{\rho_{v,p}} - 4.2424 \\ \text{or} \\ 16.8 \end{cases} \quad (10)$$

The choice of E_L value for artificial beams has limited importance because relative comparisons were made, however, the choice of a value of 16.8 GPa was consistent with the Douglas fir LVL experimental data.

E_L values also drove other material properties such as transversal and shear modulus. Indeed, E_T, the MoE in the orthogonal direction to the local direction of the fibre in LT orthotropic plane was computed from a constant $\frac{E_T}{E_L}$ ratio. This ratio was taken equal to 0.050, as proposed in Kretschmann (2010) for Douglas fir and confirmed by a reverse identification performed on the Douglas fir LVL beams (Duriot 2021). G_{LT}, the shear modulus in TL orthotropic plane was also computed assuming a constant $\frac{G_{LT}}{E_L}$ ratio. The value of this ratio was set at 0.050, resulting from the same reverse identification (Duriot 2021). Finally, ν_{LT}, the Poisson's ratio in LT orthotropic plane was taken equal to 0.449, as proposed in Kretschmann (2010).

For both BT and FE models, the beams were subdivided with a 1 mm x 1 mm grid. For each element of the grid, the material compliance matrix $[S_{v,p}]$ was transformed by a rotation of angle $\theta(x,y)$ by application of Equation (3) to obtain the local compliance matrix $[S'_{v,p}]$ in the beam xy-system for each (x,y) location of a veneer v of a ply p of the composite beam.

2.3.2 Isotropic elastic behaviour of knots

In knot areas, material properties were considered to be isotropic. For artificial beams, the knot area was defined by knot circle diameter. For the modelling of LVL beams from experimental data, the surfaces of the knots were manually segmented from grayscale images of each veneer taken from the local fibre orientation measuring device cameras. Additional information about this step is provided in Duriot et al. (2021a). Finally, for each 1 mm x 1 mm element considered as a knot (Fig. 3), the compliance matrix describing elastic properties in knots $[S_{v,p,k}]$ is that of Equation (11):

$$[S_{v,p,k}] = \begin{bmatrix} \frac{1}{E_T} & -\frac{\nu_{TT}}{E_T} & 0 \\ -\frac{\nu_{TT}}{E_T} & \frac{1}{E_T} & 0 \\ 0 & 0 & \frac{2(1+\nu_{TT})}{E_T} \end{bmatrix} \quad (11)$$

ν_{TT} was taken equal to ν_{LT} of clear wood, and E_T values were set to 0.050 of E_L value of clear wood.

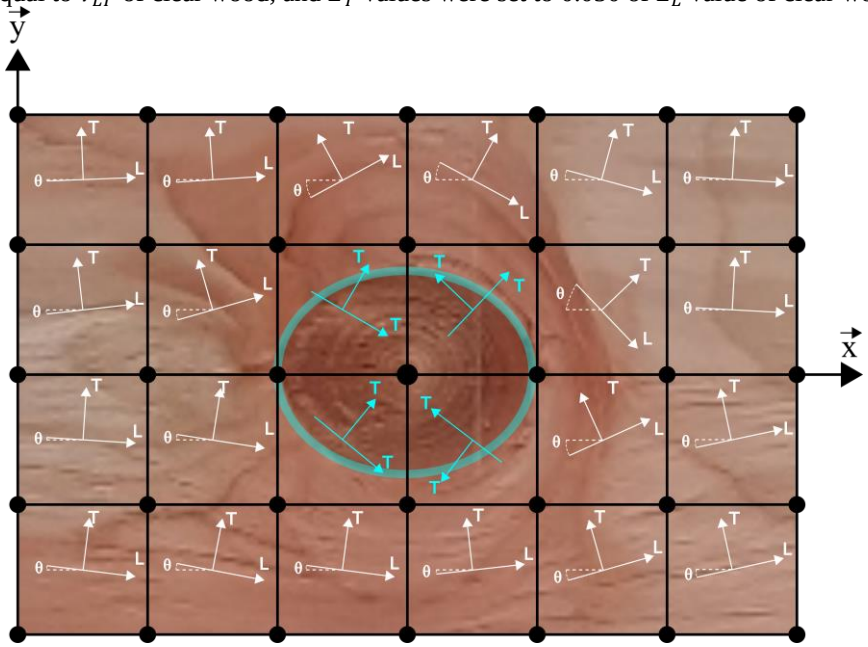

Fig. 3. Modelling principle by FE method with quadrangular plane elements in which local fibre orientation and associated local orthotropic system of axes varies (note that the central knot area shows T-direction to times to refer to isotropic material properities).

2.4 Classical analytical beam theory modelling

Depending on the number of plies in LVL modelling (n_p plies) or artificial beam modelling ($n_p = 1$ ply), a modulus in the longitudinal x-direction of the beam $E_{x,p}(x,y)$ was computed, for each (x,y) position according to the fibre angle $\theta(x,y)$ by means of (Equation (4)) with the previously defined material properties and a grid resolution of 1 mm × 1 mm. Then, an average modulus was computed as:

$$E_x(x,y) = \frac{1}{n_p}\sum_{p=1}^{n_p} E_{x,p}(x,y) \quad (12)$$

Which is like performing an integration in z-direction. Fig. 4 illustrates the E_x value obtained for an artificial beam in the knot area for an artificial beam with the knot centred in the beam depth.

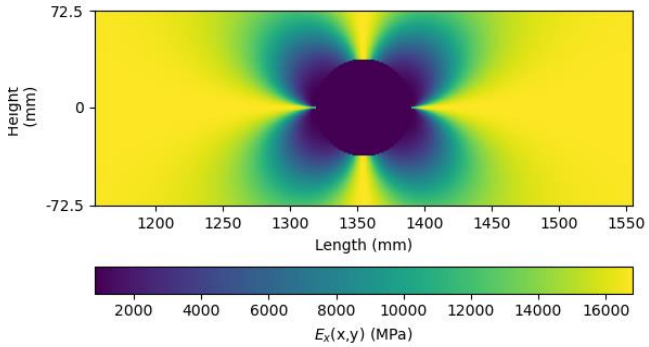

Fig. 4. E_x around knot area for an artificial beam with a knot centred in the beam depth

2.4.1 Axial loading case

Since experimental LVL beams were tested in bending only, axial loading was studied for artificial beams only. From the lengthwise modulus $E_x(x, y)$ of Equation (12), the localized axial MoE was computed at each x lengthwise position accordingly to BT as in Briggert et al. (2020) (Equation (6)), but with no longer need to integrate along z-direction:

$$E_{a,BT}(x) = \frac{1}{h}\int_{-h/2}^{h/2} E_x(x, y)dy \tag{13}$$

This computation was performed by numerical integration with dy = 1 mm. When performing this integration, the heterogeneity of the beam along y-direction is averaged to obtain a single MoE for each x-cross-section, which implies that the beam is considered isotropic and that classical BT assumptions apply.

2.4.1.1 Displacements

The longitudinal displacement obtained by BT in the local MoE area was computed as:

$$u_{x,l,BT}(x) = \int_{x_{l,min}}^{x} \frac{\sigma}{E_{a,BT}(\xi)}\, d\xi \tag{14}$$

by numerical integration with $d\xi$ = 1 mm, and with σ the input axial stress equal to 1 MPa. σ value was chosen in accordance with the FE modelling, and its sign was arbitrary chosen positive, thus inducing tension, but of course it does not impact axial MoE values in elasticity. $x_{l,min}$ is the x position of the start point of local MoE calculation as defined in EN 408 (2012) ($x_{l,min} = \frac{L}{2} - \frac{5h}{2}$, see Fig. 1). By doing so, $u_{x,l,BT}(x_{l,min}) = 0$, which is made for the sake of simplicity because it is the central area of the beams which is of interest, where the knot is located and the local MoE is computed. By using the displacement at $x_{l,min}$ as a reference, the plotted displacement curves will start at 0, which is convenient.

2.4.1.2 Averaged MoE

The averaged localized axial MoE $E_{a,avg,\delta,BT}(x)$ (the term localized will be skipped in the following for the sake of simplicity), was computed following the method of Briggert et al. (2020), *i.e.* smoothing $E_{a,BT}(x)$ by averaging it over a sliding window of length δ:

$$E_{a,avg,\delta,BT}(x) = \frac{1}{\delta}\int_{x-\delta/2}^{x+\delta/2} E_{a,BT}(\xi)\, d\xi \tag{15}$$

Equation (15) was computed by numerical integration with $d\xi$ = 1 mm. Several values of δ were taken: 10, 90 and 150 mm. The 90 mm window size was used by Olsson et al. (2018) and Hu et al. (2022) while the 150 mm window size was classically used for the widely known knot area ratio and used by Rais et al. (2021) for determining a

criterion based on fibre angle scanning. The 10 mm size has been chosen to be considerably lower than the two other sizes, but still containing several elements (10 of them since the element size is 1 mm).

2.4.1.3 Apparent MoE

It is proposed in the present paper to compute the localized axial MoE from the displacements, $E_{a,app,\delta,BT}(x)$. This MoE is called in the present paper "apparent MoE", as it can be seen as the MoE that would be observed if a mechanical test could be done within a short portion of the beam, of length δ. Thus, this apparent axial MoE can be computed as:

$$E_{a,app,\delta,BT}(x) = \sigma \frac{\delta}{u_{x,l,BT}\left(x+\frac{\delta}{2}\right) - u_{x,l,BT}\left(x-\frac{\delta}{2}\right)} \tag{16}$$

It's worth noting that this approach based on the displacements gives a different formula than what is done when simply smoothing the localized MoE by averaging it like in Equation (15). Indeed, developing Equation (16) with the help of Equation (14) gives:

$$\begin{aligned} E_{a,app,\delta,BT}(x) &= \sigma\delta / \left(\int_{x_{l,min}}^{x+\frac{\delta}{2}} \frac{\sigma}{E_{a,BT}(\xi)}\, d\xi - \int_{x_{l,min}}^{x-\frac{\delta}{2}} \frac{\sigma}{E_{a,BT}(\xi)}\, d\xi \right) \\ &= \sigma\delta / \left(\int_{x_{l,min}}^{x+\frac{\delta}{2}} \frac{\sigma}{E_{a,BT}(\xi)}\, d\xi + \int_{x-\frac{\delta}{2}}^{x_{l,min}} \frac{\sigma}{E_{a,BT}(\xi)}\, d\xi \right) = \delta / \int_{x-\frac{\delta}{2}}^{x+\frac{\delta}{2}} \frac{1}{E_{a,BT}(\xi)}\, d\xi \end{aligned} \tag{17}$$

Hence, compared to the averaged axial MoE of Equation (15) which is an arithmetic average, the apparent axial MoE is the harmonic average of the localized MoE, *i.e.* the equivalent stiffness of a spring of length δ composed of springs in series of individual stiffnesses $E_{a,BT}(x)$.

2.4.1.4 Local MoE

As stated in the introduction, the local MoE as defined in EN 408 (2012) in a tensile test is supposed to be measured in the central area of the specimen over a distance of $5h$. In the present BT modelling of artificial beams, it corresponds to using the displacements computed at $x_{l,min}$ and $x_{l,max}$ positions (see Fig. 1). As a result, the local MoE under axial loading, $E_{a,l,BT}$, is neither but a particular case of apparent MoE, computed as:

$$E_{a,l,BT} = \sigma \frac{5h}{u_{x,l,BT}(x_{l,max}) - u_{x,l,BT}(x_{l,min})} \tag{18}$$

2.4.2 Bending loading case

The effective bending stiffness along the beam was computed as:

$$EI_{eff}(x) = t \int_{-h/2}^{h/2} E_x(x,y)\left(y - \overline{y(x)}\right)^2 dy \tag{19}$$

by numerical integration with dy = 1 mm.

2.4.2.1 Displacements

Beam deflection in bending was computed by applying the unit-load or virtual work method (Fuchs, 2016). It allows to compute the deflection of a beam subjected to a bending moment M in a specific x location by associating it with a similar system in terms of boundary conditions, but subjected to a virtual unit load in the desired location, which induce a bending moment M_x. The problem is then reduced to calculating the integral along the beam of the product of the two bending moments divided by the effective bending stiffness. In the present case, the

deflection at the start point of local MoE calculation is also subtracted to the global deflection for a better representation, as explained in 2.4.1.1 for the axial loading case, which gives $u_{y,l,BT}(x)$:

$$u_{y,l,BT}(x) = \int_0^L \frac{M(\xi)M_x(\xi)}{EI_{eff}(\xi)}d\xi - \int_0^L \frac{M(\xi)M_{x_{l,min}}(\xi)}{EI_{eff}(\xi)}d\xi \quad (20)$$

where M is the bending moment distribution along x-direction due to the four-point bending loading corresponding to a theoretical maximum bending stress of 1 MPa for a homogenous beam, M_x is the bending moment distribution induced by a unit load at the desired x position where the displacement is computed, and $M_{x_{l,min}}$ is the bending moment distribution induced by a unit load at $x_{l,min}$ position.

2.4.2.2 Averaged MoE

The localized MoE in bending at each x lengthwise position, $E_{b,BT}(x)$ was computed following BT as in Equation 5 from Olsson et al. (2013). Then, the averaged bending MoE $E_{b,avg,\delta,BT}(x)$, was computed still following the method of Olsson et al. (2013), *i.e.* by averaging $E_{b,BT}(x)$ over a sliding window of length δ:

$$E_{b,avg,\delta,BT}(x) = \frac{1}{\delta}\int_{x-\delta/2}^{x+\delta/2} E_{b,BT}(\xi)\, d\xi \quad (21)$$

Equation (21) was computed by numerical integration with $d\xi$ = 1 mm and with the same δ values as in the axial loading case.

2.4.2.3 Apparent MoE

As in the axial loading case, it is proposed to compute the localized bending MoE from the displacements, named apparent bending MoE, $E_{b,app,\delta,BT}(x)$. For this purpose, a curvature $\chi_{\delta,BT}(x)$ was computed by fitting a circle through the three points of coordinates $\left(x-\frac{\delta}{2}\,;\, u_{y,l,BT}\left(x-\frac{\delta}{2}\right)\right)$, $\left(x\,; u_{y,l,BT}(x)\right)$, and $\left(x+\frac{\delta}{2}\,;\, u_{y,l,BT}\left(x+\frac{\delta}{2}\right)\right)$. Finally, the apparent bending MoE obtained by this method is:

$$E_{b,app,\delta,BT}(x) = \frac{M}{\chi_{\delta,BT}(x)\, I} \quad (22)$$

where M is the applied four-point bending moment which was constant between the $x_{l,min}$ and $x_{l,max}$ positions within which the apparent MoE was computed.

2.4.2.4 Local MoE

As in the axial loading case, under bending loading, the local MoE is also a particular case of the apparent MoE. In this particular case, the curvature can be computed from the deflection Δu_y between the $x_{l,min}$ and $x_{l,max}$ positions and the middle position x_c (see Fig. 1), as proposed in EN 408 (2012). Thus, the local MoE in bending following BT modelling, $E_{b,l,BT}$, was computed as:

$$E_{b,l,BT} = \frac{(5h)^2\, M}{8\, I \Delta u_y} \quad (23)$$

with the deflection Δu_y computed as:

$$\Delta u_y = \frac{u_{y,l,BT}(x_{l,max}) + u_{y,l,BT}(x_{l,min})}{2} - u_{y,l,BT}(x_c) \quad (24)$$

2.5 Finite element modeling

2.5.1 Model building

The FE model developed in this study simulates the four-point bending and axial tensile test in two dimensions in the LT plane under plane stress conditions. This modelling choice is justified by the fact that only the in-plane fibre angles were taken into account.

Cast3m (CEA 2018) FE software has been used in the present study. The chosen element type was "QUA4", which are four node elements with linear interpolation. Element size was 1 mm × 1 mm (*i.e.* the same grid size as BT modelling and fibre angle data). Each element had its own elementary stiffness matrix in the xy-global system depending on the local fibre orientation and computed from the compliance matrix $[S'_{v,p}]$, as defined before and as illustrated in the mesh grid of Fig. 3. Note that FE modelling took in input exactly the same material properties as BT modelling.

2.5.2 Total global stiffness matrix construction

For each veneer, the stiffness matrix $[K_{v,p}]$ was calculated by assembling all the elementary stiffness matrices of each element composing the veneer. For LVL, it was considered that each ply, assembly of several veneers in the beam length, constituted a single mesh of finite elements, as if there was perfect continuity from one veneer to another. Thus, the stiffness matrices of each ply, $[K_p]$, were constituted from stiffness matrices of the veneers. Finally, the total global beam stiffness matrix $[K]$ was constituted by the sum of the n_p ply stiffness matrix $[K_p]$ as in Equation (25):

$$[\mathrm{K}] = \sum_{p=1}^{n_p} [K_p] \tag{25}$$

2.5.3 Axial loading case

2.5.3.1 Loading and boundary conditions

The boundary conditions for the axial loading case on the artificial beams are described in Fig. 5. They are composed of $u_x = 0$ displacements at coordinate $x = 0$ (u_x being the component of displacement in the x-direction) and $u_y = 0$ displacement at the coordinate points $(x = 0;\ y = 0)$ and $(x = L;\ y = 0)$ (u_y being the component of displacement in the y-direction). The boundary condition in y-direction aims to prevent displacements in this direction due to heterogeneity and orthotropic behaviour of beams with non-centred knots. A tensile stress of σ = 1 MPa is uniformly distributed to the $x = L$ coordinate segment.

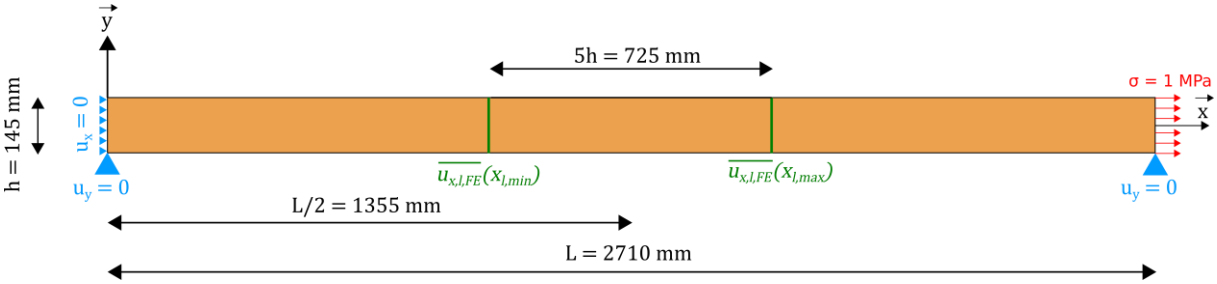

Fig. 5. Boundary conditions for FE axial loading

2.5.3.2 Displacements

Displacement components were calculated at each element by solving with Cast3m (CEA 2018) software the equilibrium equation $\{F\} = [\mathrm{K}]\{u\}$ with $\{F\}$ the generalized force vector and $\{u\}$ the generalized displacement vector.

For each beam, $\overline{u_{x,l,FE}}$ the component of displacement in the x-direction averaged in y-direction with the displacement at $x_{l,min}$ as a reference was calculated from the FE output displacements u_x by numerical integration with dy = 1 mm according to Equation (26):

$$\overline{u_{x,l,FE}}(x) = \frac{1}{h}\int_{-\frac{h}{2}}^{\frac{h}{2}} u_x(x,y) - u_x(x_{l,min},y)\ dy \tag{26}$$

The FE lengthwise displacement from this equation aims to be comparable to the BT lengthwise displacement. Moreover, the averaging in y-direction seemed necessary because if a particular y line was chosen, the results would have been highly dependent on the y position of the line relatively to knot y_k position.

2.5.3.3 Apparent MoE

Two methods have been previously described in the BT modelling to compute a localized MoE: directly averaging the input MoE computed from fibre angle data, or computing an apparent MoE by post-processing the displacements obtained after the application of BT mechanics. For FE modelling, only post-processing is possible. It can be performed on the basis of the displacements to compute an apparent MoE, $E_{a,app,\delta,FE}$ similarly to the BT case of Equation (16):

$$E_{a,app,\delta,FE}(x) = \sigma\frac{\delta}{\overline{u_{x,l,FE}}(x+\frac{\delta}{2}) - \overline{u_{x,l,FE}}(x-\frac{\delta}{2})} \tag{27}$$

2.5.3.4 MoE from averaged strains

Instead of using the displacements, another way is to use the lengthwise strains and apply BT formulae as it was done in several literature articles for bending (Hu et al. 2018; Lukacevic et al. 2019; Huber et al. 2022). In the present axial loading case, the lengthwise strains ε_{xx} were averaged along $\vec{y}$ for each x position. This gives $\overline{\varepsilon_{xx}}(x)$, the averaged longitudinal strain. Then, the localized axial MoE was computed as:

$$E_{a,\varepsilon,\delta,FE}(x) = \sigma\frac{\delta}{\int_{x-\delta/2}^{x+\delta/2}\overline{\varepsilon_{xx}}(\xi)\,d\xi} \tag{28}$$

by numerical integration with $d\xi$ = 1 mm.

2.5.3.5 Local MoE

The local MoE under axial loading computed from FE modelling, $E_{a,l,FE}$, was computed in the same way as in the BT modelling (Equation (18)), but by using $\overline{u_{x,l,FE}}$, the lengthwise displacement averaged along y-direction:

$$E_{a,l,FE} = \sigma\ \frac{5h}{\overline{u_{x,l,FE}}(x_{l,max}) - \overline{u_{x,l,FE}}(\,x_{l,min})} \tag{29}$$

Here, another choice could have been made, like taking the displacement at the centre line of the beam ($u_{x,l,FE}(x, y = 0)$), which would correspond to what is advised to use in EN 408 (2012) standard. However, it has been preferred to use the lengthwise displacement averaged along y-direction to be consistent with the apparent MoE calculation. In practice this is of little importance as the consequences in terms of local MoE value were not significant and not worth discussing in the present paper.

2.5.3.6 Tsaï-Hill equivalent strength

The equivalent strength obtained by application of Tsaï-Hill criterion in tension, $f_{t,eq}(x,y)$, was computed as proposed by Grazide et al. (2018) (Equation (9)), with the same strength parameters, *i.e.* $f_{t,L}$ = 90 MPa the tensile strength in the longitudinal direction of the fibre, $f_{t,T}$ = 4 MPa the tensile strength in the tangential direction of the fibre, f_v = 10 MPa the shear strength in LT plane (and σ = 1 MPa the applied loading). Although being chosen quite arbitrarily, these strength values are of correct order of magnitude for Douglas fir. In the knot area, the criterion has been discarded ($f_{t,eq}(x,y)$ set equal to $f_{t,L}$ for practical purpose), so the lowest equivalent strength was never found within the knot but around it, due to fibre deviation.

2.5.4 Bending loading case

2.5.4.1 Loading and boundary conditions

The bending behaviour was studied for artificial and experimental LVL beams in their central area, *i.e.* the area subjected to pure bending. For LVL beams, which were optimized favourably or unfavourably, it is in this area that highly contrasted plies in terms of material properties values (density, local fibre orientation) were concentrated depending on the optimization configuration.

To model the bending in the FE model, a load was applied to the mesh on a length of 40 mm to meet the experimental test conditions. Fig. 6 shows the boundary conditions applied to the beam for FE calculation. The loads q have been computed so they induce a maximum longitudinal stress of 1 MPa for a homogeneous beam. The beam u_y displacements were blocked at the coordinate points $(x = 50;\ y = 0)$ and $(x = L - 50;\ y = 0)$ corresponding to contact segment centres of the beam with the lower supports. A displacement relationship was applied to the elements in contact with segments delineating the lower supports, with the objective to model the rotation allowed in the test configuration by the pivot-mounted supports. Finally, the point $\left(x = x_c = \frac{L}{2};\ y = 0\right)$ was blocked according u_x displacement so the possible longitudinal displacements were centred.

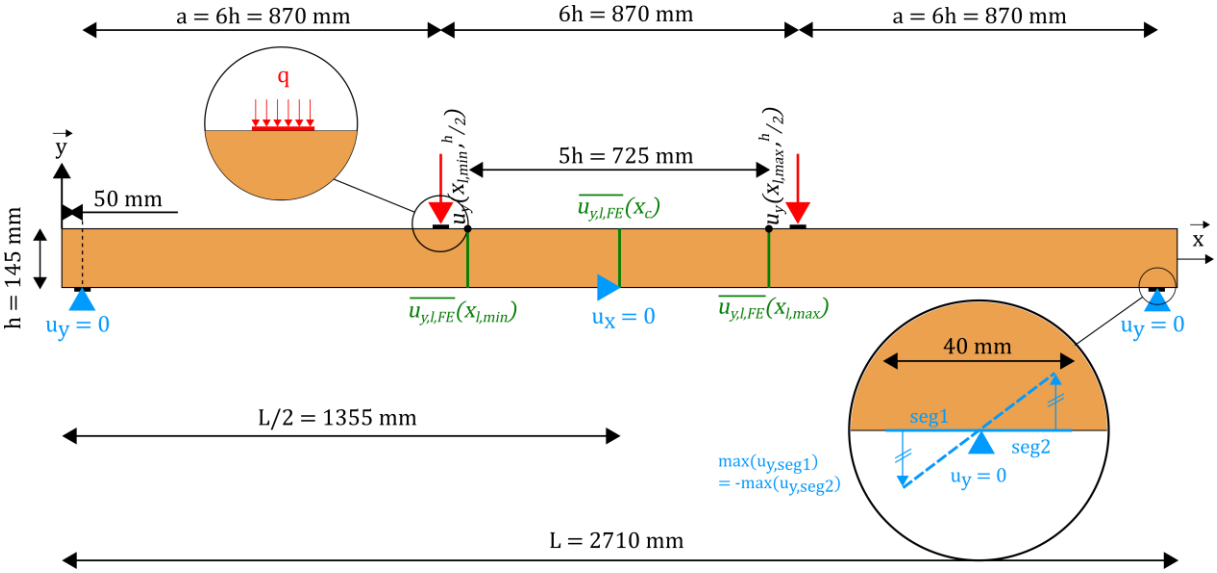

Fig. 6. FE modelling boundary conditions and position of vertical displacement calculation points for four points bending loading case

2.5.4.2 Displacements

Similarly to the axial loading case, here $\overline{u_{y,l,FE}}$, the component of displacement in the y-direction averaged in the y-direction with the displacement at $x_{l,min}$ as a reference, was calculated from the FE output displacements u_y according to Equation (30):

$$\overline{u_{y,l,FE}(x)} = \frac{1}{h}\int_{-h/2}^{h/2} u_y(x,y) - u_y(x_{l,min},y)\,dy \tag{30}$$

by numerical integration with dy = 1 mm.

2.5.4.3 Apparent MoEs

Before being processed, $\overline{u_{y,l,FE}}(x)$ needed to be slightly smoothed by splines (spaps function of MATLAB®) to reduce noise, giving $\widehat{\overline{u_{y,l,FE}}}(x)$. Then, a curvature $\chi_{\delta,FE}(x)$ was computed by fitting a circle through the three points of coordinates $\left(x-\frac{\delta}{2}\,;\,\widehat{\overline{u_{y,l,FE}}}\left(x-\frac{\delta}{2}\right)\right)$, $\left(x\,;\widehat{\overline{u_{y,l,FE}}}(x)\right)$, and $\left(x+\frac{\delta}{2}\,;\,\widehat{\overline{u_{y,l,FE}}}\left(x+\frac{\delta}{2}\right)\right)$. Finally, the apparent MoE in bending obtained by this method is:

$$E_{b,app,\delta,FE}(x) = \frac{M}{I\,\chi_{\delta,FE}(x)} \tag{31}$$

2.5.4.4 MoE from averaged strains

Another localized bending MoE was computed from the strains according to Hu et al. (2018) method. $\widehat{\varepsilon_{xx}}(x,y)$, the linear approximated longitudinal strain was computed for each x position by linear regression of the lengthwise strains ε_{xx} along $\vec{y}$. Then it was used to compute the localized bending MoE obtained from strains as in Equation (8) but by averaging the $\frac{\partial\widehat{\varepsilon_{xx}}}{\partial y}$ slope within the sliding-window of length δ:

$$E_{b,\varepsilon,\delta,FE}(x) = \frac{M}{I\int_{x-\delta/2}^{x+\delta/2}\frac{\partial\widehat{\varepsilon_{xx}}(\xi)}{\partial y}\,d\xi} \tag{32}$$

2.5.4.5 Local MoE

As in the axial loading case, the local MoE under bending loading computed from FE modelling, $E_{b,l,FE}$, was also computed in the same way as in the BT modelling (Equation (23)). However, in the case of artificial beams, the deflection Δu_y was computed by using $\overline{u_{y,l,FE}}$, the y displacement averaged along y-direction:

$$\Delta u_y = \frac{\overline{u_{y,l,FE}}(x_{l,max}) + \overline{u_{y,l,FE}}(x_{l,min})}{2} - \overline{u_{y,l,FE}}(x_c) \tag{33}$$

The choice to use the y displacement averaged along y-direction instead of the y displacement at the centre line of the beam ($u_{y,l,FE}(x, y=0)$), was made for the same reasons as in the axial loading case and had non-significant consequences in the following discussions as well.

However, in the case of the FE modelling of LVL beams that were tested experimentally, the choice was made to use the displacement at the same $y = h/2$ location as in the experimental test (see Fig. 6), which gives:

$$\Delta u_y = \frac{u_y\left(x_{l,max},\frac{h}{2}\right) + u_y(x_{l,min},h/2)}{2} - u_y\left(x_c,\frac{h}{2}\right) \tag{34}$$

2.5.4.6 Tsaï-Hill equivalent strength

The equivalent strength obtained by application of Tsaï-Hill criterion in bending, $f_{b,eq}(x,y)$, was computed in the same way as $f_{t,eq}(x,y)$, with the same parameters. It could be discussed that compressive and tensile strength should be different, but it is not studied in the present work, for which the knots were positioned in the tension part of the bent beam.

2.6 Experimental local MoE for LVL beams

The Douglas fir LVL beams described in section 2.2.2 were tested in the four-point bending test configuration of Fig. 6 which follows the recommended span and loading heads position of EN 408 (2012) standard. Their local MoE, $E_{b,l,exp}$, was computed as in Equation (23) but by replacing the moment M by the increment of moment measured during the bending test between 10 % and 40 % of the maximum load, and Δu_y by the corresponding increment of deflection, as advised in EN 408 (2012$y = h/2$

3. Results and discussion

3.1 Comparison of beam theory and finite element modelling methods in terms of displacements and apparent MoEs

Fig. 7 shows the averaged displacements observed in axial tension and pure bending in the area of local MoE measurement in the sense of EN 408 (2012), which means in the central part of the specimen between $x_{l,min}$ and $x_{l,max}$ positions (which corresponds to a length of 725 mm). Fig. 8 and Fig. 9 show the corresponding apparent MoE profiles, *i.e.* localized MoEs computed from the displacement across different sliding window lengths. In all the Figures, the FE and BT modelling are displayed with the different line styles given in Table 2, with different colours for the different artificial beams (*i.e.* different knot y_k positions). The homogeneous artificial beam is named “no knot”. It was verified that for the homogeneous artificial beam the displacements and thus apparent MoEs were identical for BT and FE modelling approaches. This artificial homogeneous beam provides a visual reference in the different figures.

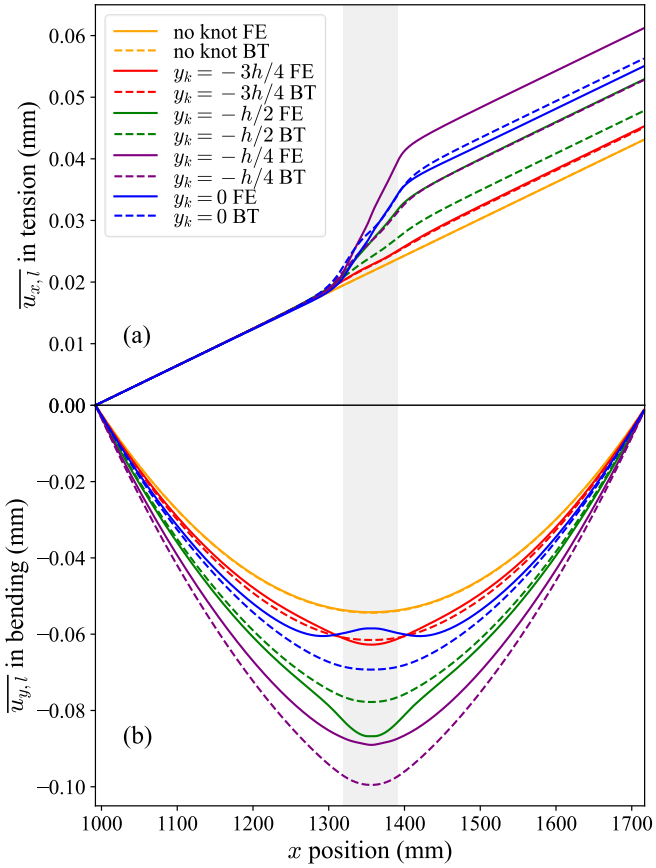

Fig. 7. Displacements averaged over beam depth (y-direction) obtained by FE (solid line) and BT modelling (dashed line) according to x position in the "5 times depth" central area of the beam, under axial tensile loading of 1 MPa (a), and a bending moment corresponding to a maximum stress of 1 MPa (b). Line colours refer to knot y_k position, the central grey rectangle represents the location and width of the knot (whose diameter was 72.5 mm). [colour version online]

Under axial loading, it can be seen in Fig. 8 that the apparent MoE logically decreased in the vicinity of the knot area whatever the y_k position of the knot in the depth of the beam, and whatever the modelling approach used. When the apparent MoE was computed over a small sliding window of 10 mm (Fig. 8 a), there was in most cases a local increase of apparent MoE when being within knot borders (grey rectangle in Fig. 8 a), which is explained by the fact that the fibres became oriented in the x-direction of the beam when being at the middle x position of the knot (see Fig. 1). This effect appeared with various intensities according to knot y_k position and modelling approach. Increasing the length of the sliding window induced a smoothing of this behaviour which disappeared for 90 mm (Fig. 8 b) and 150 mm (Fig. 8 c) sliding window lengths. The other expected consequences of increasing sliding window length were an enlargement of the size of the area affected by the knot along $\vec{x}$, and an increase of the minimum apparent MoE values. However, the order of the curves remains the same, *i.e.* the relative differences in apparent MoE between the different knot y_k positions and modelling approaches were not highly affected by sliding window length. It can be observed both in the displacements (Fig. 7 a) and the apparent MoE profiles (Fig. 8) that FE and BT modelling were similar for knot position $y_k = -\frac{3h}{4}$, and $y_k = 0$, but very different for knot positions $y_k = -\frac{h}{4}$, and $y_k = -\frac{h}{2}$, the FE model being more compliant. This will be discussed in the next section by the analysis of local MoE.

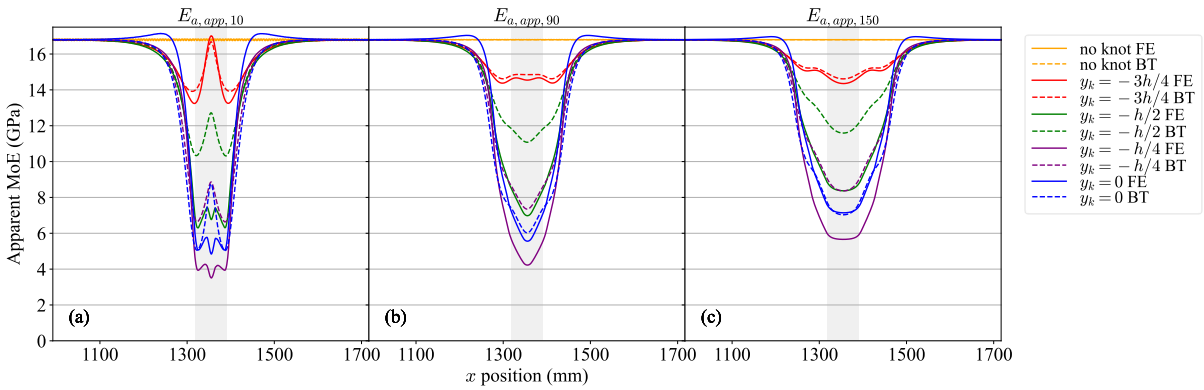

Fig. 8. Apparent MoE under axial loading obtained by FE (solid line) and BT modelling (dashed line) according to x position in the "5 times depth" central area of the beam, computed in 10 mm (a), 90 mm (b), and 150 mm (c) long sliding windows. [colour version online]

In bending, it can be seen that in terms of displacements (Fig. 7 b), the FE and BT models were close only in the case of the artificial beam with the knot positioned at $y_k = -\frac{3h}{4}$, *i.e.* the one for which the fibre deviations were minimum (apart, of course, from the case of the homogeneous beam, for which the results were identical). The displacement curves also show a much more complex behaviour in the FE model than in the BT model, with the curvature varying more for the FE model, and even changing of sign. For example, for the artificial beam with the knot centred ($y_k = 0$), it can be seen in Fig. 7 b that in the central x position, where the center of the knot was located, the curvature was locally in the opposite direction to the global curvature of the beam in bending. Because the apparent MoE was computed from the curvature through 3 points (Equation (31)), these kind of variations of curvature sign induce discontinuities in the apparent MoE profiles computed from FE modelling, which is the reason why it can appear infinite if a short sliding window length is considered, as shown in Fig. 9 a and b for 10 mm and 90 mm sliding window size, respectively. This behaviour makes difficult the analysis of these Figures, but the variations of apparent MoE were much easier to observe when the curvature was computed with a 150 mm long sliding window (Fig. 9 c), thanks to the higher smoothing. The computed curvature in this case still induced locally very high apparent MoE values for beams with knots when using FE modelling (much higher than 16.8 GPa, which is the fibres' MoE in their main longitudinal direction). Obtaining apparent MoE values higher than the material longitudinal MoE could appear surprising, but this is the direct translation of a local curvature that is affected around the knot by coupling phenomena due to the orthotropic nature of the material. The strain maps provided in supplementary materials show this complexity.

On the opposite to FE modelling, the displacements obtained from BT modelling kept a smoother curvature (Fig. 7 b) and the resulting apparent MoE profiles behaved more like in the axial loading case, never exceeding the fibres' MoE in longitudinal direction (Fig. 9).

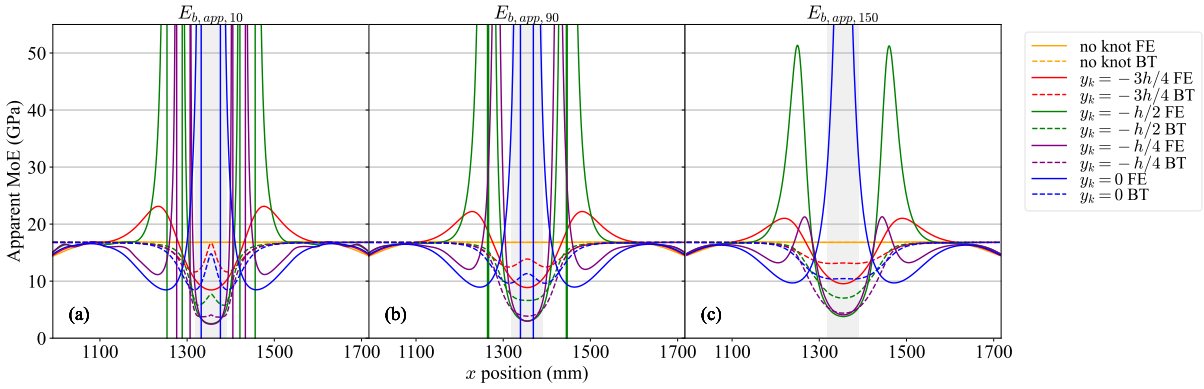

Fig. 9. Apparent MoE in bending obtained by FE (solid line) and BT modelling (dashed line) according to x position in the "5 times depth" central area of the beam, computed in 10 mm (a), 90 mm (b), and 150 mm (c) long sliding windows. [colour version online]

3.2 Local MoE

3.2.1 Artificial beams

Fig. 10 shows the obtained local MoEs in axial and bending loadings, both obtained by FE and BT modelling according to the y_k position of the knot in the depth of the beam. As in the other Figures, the results with no knot, *i.e.*, for a homogeneous beam, are also displayed for reference, the local MoE being the input MoE of 16.8 GPa.

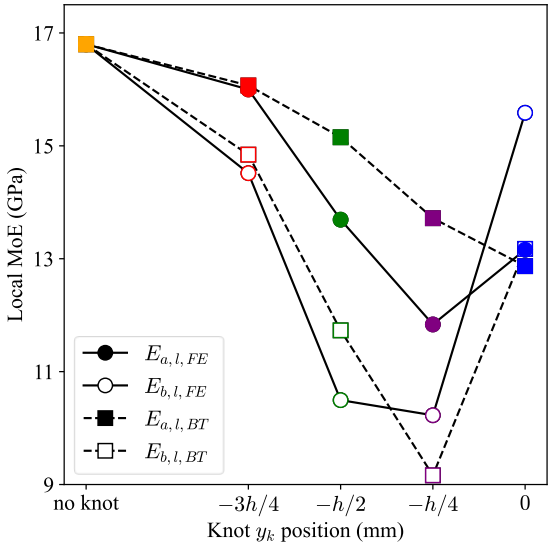

Fig. 10. Evolution of local MoE in axial loading (filled markers) and bending loading (empty markers) according to knot y_k position obtained by FE (solid line) and BT modelling (dashed line). The abscissa of the "no knot" beam has been set arbitrarily. Marker colours correspond to different knot y_k positions as in other Figures.

Apart from the case for which the knot was centred in the middle line of the board ($y_k = 0$), the local MoE was lower in bending than in axial loading whatever the model considered. The ratios $E_{a,l}/E_{b,l}$ were equal to 1.10, 1.30, 1.16 and 0.84 for knot positions $y_k = -3h/4$, $y_k = -h/2$, $y_k = -h/4$ and $y_k = 0$, respectively. The difference between axial and bending MoE has been discussed in a few experimental studies: Burger and Glos (1995) found a relationship of E_b/E_a = 1.09 on 147 specimens of Norway spruce, but Steiger and Arnold (2009) found exactly the inverse (at most for the lowest qualities), E_a/E_b = 1.09, on a larger scale study (1492 specimens of various cross sections). The present modelling results show that the difference between axial and bending MoE is highly dependent on knot position, which may explain mixed experimental results depending on the knot positions distribution.

These differences between axial and bending behaviours can be explained with a BT reasoning: when the knot is not centred across $\vec{y}$, its lower mechanical properties are away from the neutral fibre and closer to the edge, thus in the area where the influence is maximum in bending. Following this reasoning, when the knot is centred in the board ($y_k = 0$), straighter fibres can be located close to the edges, and thus the localized MoE in bending can be higher than when the knot is not centred, despite that there is a higher proportion of knot relatively to the cross-section. Conversely, under axial loading, the local MoE can only be decreasing with the proportion of knot in the cross-section, because there is no effect of the distance to neutral fibre. These behaviours can be observed in Fig. 10 in the evolution of the BT curves with knot position.

The previous reasoning, however, does not explain how the local MoE under axial loading obtained by FE modelling is significantly higher if the knot is centred ($y_k = 0$) than if it is at $y_k = -h/4$. FE modelling accounts for the full tensor of stresses and strains according to the local fibre orientation in a way that a BT reasoning cannot. Thus, FE modelling is of course more representative of the actual MoE than BT modelling. In the particular example of the knot centred on the middle line of the beam, it should be remarked that in this configuration the fibres are oriented around the knot in somehow the optimal direction according to the direction of the principal stresses that would exist in a homogeneous beam with a hole of the diameter of the knot, which certainly explains the surprisingly stiff behaviour. The reader can observe the full maps of strains in the supplementary material to see in detail the difference between artificial beam strain maps.

The differences between FE and BT modelling were variable according to knot position and loading type. When there were relatively low deviations of fibres and the knot was not included in the board, there was a relatively low difference in terms of modelled local MoE between BT and FE modelling (limited to 2.3 % in bending when $y_k = -\frac{3h}{4}$). Conversely, when the knot was included in the board and thus the mechanical behaviour was more complex to get with BT, the differences could be significant, in either direction: for a knot located at $y_k = -\frac{h}{4}$ under axial loading, the local MoE obtained with BT modelling was 15.9 % higher than FE modelling, whereas for a knot located at $y_k = -\frac{h}{4}$ under bending loading, the local MoE obtained with BT modelling was 10.4 % lower than FE modelling.

3.2.2 Experimental LVL beams

For the artificial beams, only one size of knot and a few knot positions have been tested, thus it is difficult to evaluate how the observed difference between BT and FE modelling would be reflected in practice. This is the reason why these modelling methods had been applied on actual LVL beams for which the fibre angles had been measured by laser dot scanning. Fig. 11 compares the local MoE measured experimentally on the Y-axis to the local MoE obtained from BT and FE modelling. The difference in local MoE between BT and FE modelling for optimized beams with minimized knottiness in the central area was smaller than for beams with maximized knottiness in the central area (2.7 % versus 6.3 % of difference). This result is thus in accordance with what was found in the case of the artificial beams, with higher difference between the models when there is more fibre deviation. The FE modelling induced higher MoEs, which were closer to the experimental results. The RMSE between $E_{b,l,FE}$ and $E_{b,l,exp}$ was equal to 0.440 GPa while it was equal to 0.776 GPa between $E_{b,l,BT}$ and $E_{b,l,exp}$. This result highlights the better accuracy of FE modelling, even if it should be confirmed with more experimental data.

Although the size and positions of the knots were much more variable in the actual beams than in the tested artificial cases, the higher local MoEs of LVL FE modelling seems consistent with the results of local MoEs of artificial beams (section 3.2.1): when there are low fibre deviations BT and FE modelling results are close, but when there are high fibre deviations they are different, with a tendency of the FE modelling to present higher stiffness in bending when the knots are embedded in the cross-section ($y_k = -h/4$ and $y_k = 0$ for artificial beams).

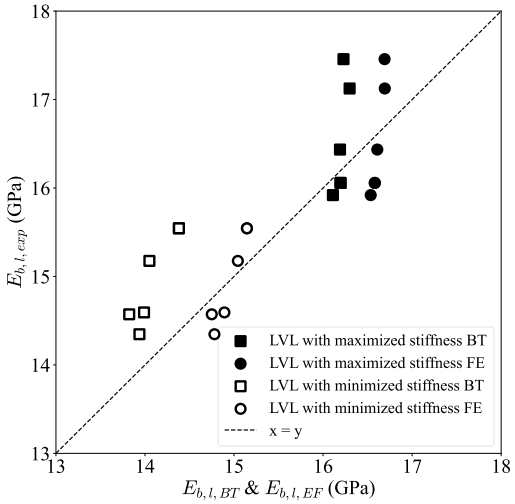

Fig. 11. Comparison between BT and FE bending local MoE versus experimental local MoE for each LVL beam

3.3 Comparison between localized MoE computation methods

The lengthwise variations of the different kinds of localized MoE profiles summarized in Table 2 are difficult to compare visually altogether, thus they are compared here only for the artificial beam with the knot located at $y_k = -\frac{h}{2}$, which allows for a good observation of the potential differences between modelling and smoothing methods.

3.3.1 Axial loading case

Fig. 12 shows the lengthwise variations of the four localized axial MoEs for the artificial beam with the knot located at $y_k = -\frac{h}{2}$. First, the FE-based apparent MoE from displacements and localized MoE from averaged strains were identical, thus they cannot be distinguished in Fig. 12. This was expected because under axial loading and for a given sliding window length, the difference in averaged displacements that are in Equation (27) is the same as the cumulated strains that are in Equation (28). It will be shown later that it is not the case under bending loading.

Secondly, the BT-based localized MoE were visually indissociable when $\delta = 10$ mm (Fig. 12a) and the difference slightly increased when increasing the sliding-window length to 90 mm and 150 mm (Fig. 12b and 13c, respectively). This effect was expected as the apparent MoE is the harmonic average of the localized MoE whereas the averaged MoE is the arithmetically averaged MoE. However, the difference appeared to be very small, even for the quite large sliding-window length of 150 mm, thus, in the frame of axial loading, the method of computation of BT-based localized MoE should not imply any significant difference when modelling timber mechanical behaviour. On the contrary, the differences between FE and BT MoEs were very large and implied totally different mechanical responses that have been already discussed and should be considered when modelling timber with knots.

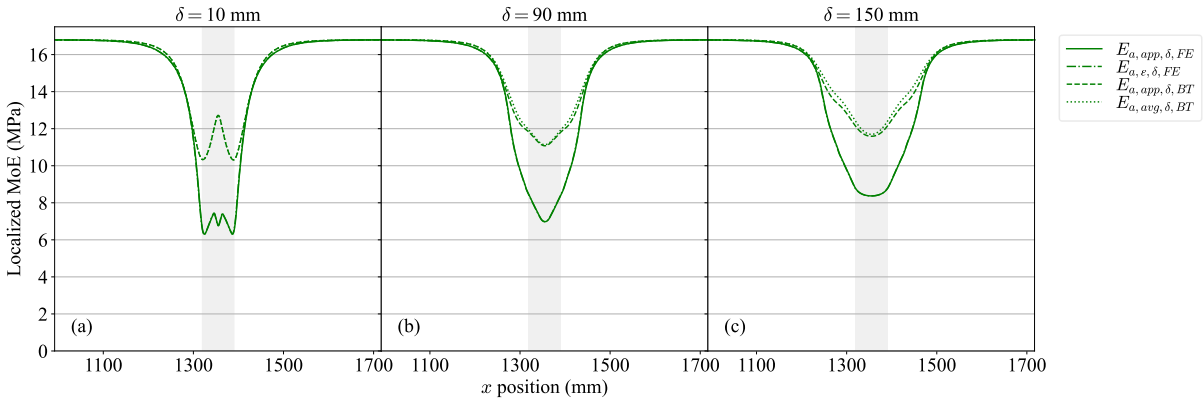

Fig. 12. Localized axial MoE comparisons in the case of the artificial beam with knot position $y_k = -\frac{h}{2}$, according to x position in the "5 times depth" central area of the beam and sliding-window lengths δ of 10 mm (a), 90 mm (b), and 150 mm (c). Note that $E_{a,app,\delta,FE} = E_{a,\varepsilon,\delta,FE}$, therefore the curves are indissociable.

3.3.2 Bending loading case

Fig. 13 shows the lengthwise variations of the four localized bending MoEs for the artificial beam with the knot located at $y_k = -\frac{h}{2}$. For the shortest sliding window of 10 mm (Fig. 13a), the two localized MoE computed by BT modelling were almost identical so it was not possible to distinguish them. However, the difference between them increased when increasing the sliding-window length to 90 mm and 150 mm (Fig. 13b and Fig. 13c, respectively), and it increased in a much more significant way than in the previously discussed axial loading case. The reason for this behaviour certainly relies on the same effect of "arithmetic versus harmonic averages", but with a greater impact due to the variation of longitudinal strains in the cross-section under bending loading.

Contrary to the axial loading case, the two computation methods of localized MoE based on FE modelling showed very different behaviours. The localized bending MoE computed from strains by FE modelling was actually quite similar to the averaged MoE obtained by BT modelling. This may be explained by the fact that Equation (8) from which the localized bending MoE computed from strains was obtained is a BT equation: it supposes that the strains ε_{xx} vary linearly over beam depth, which is not the case in the knot area, as it was shown by Hu et al. (2018) and in the present supplementary materials. The linear regression results in a strong smoothing of the variation of strains.

The radical differences between FE and BT apparent MoEs were already discussed before. Despite the erratic variations of apparent MoE obtained by FE modelling, it can be noticed that the minimum value in the central area

behaved similarly to the other localized MoE, which is an interesting behaviour that will be used in the next section. It also appeared when comparing Fig. 13a to Fig. 13c that the minimum localized MoE computed from the strains by FE modelling was more impacted by the sliding-window length than the apparent MoE computed from FE modelling.

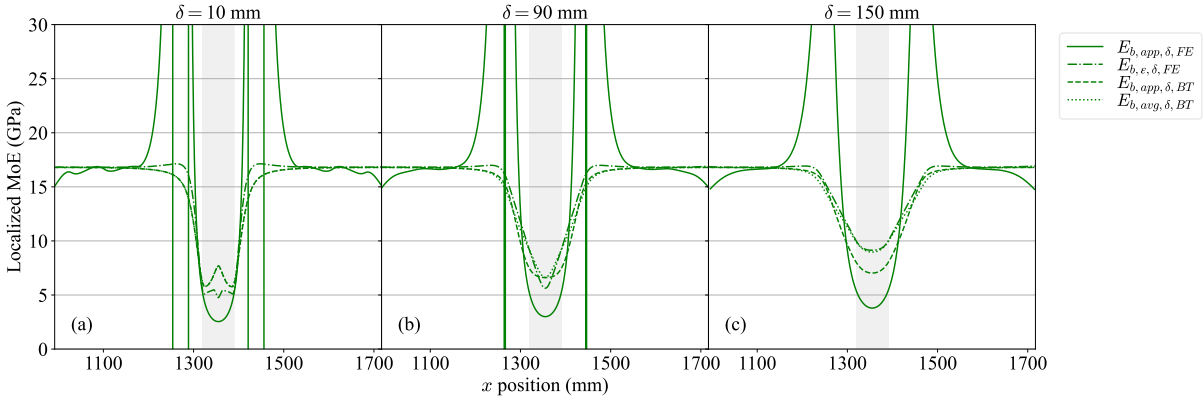

Fig. 13. Localized bending MoE comparisons in the case of the artificial beam with knot position $y_k = -\frac{h}{2}$, according to x position in the "5 times depth" central area of the beam and sliding-window lengths δ of 10 mm (a), 90 mm (b), and 150 mm (c).

3.4 Minimum localized MoE for strength prediction

As stated in the introduction, several authors used a localized MoE or another criterion as a predictor of mechanical strength, looking for the minimum value (smoothed by a sliding window) along board length. The minimum localized MoEs have been searched for each artificial beam, each localized MoE and each sliding window length, and they are presented in Fig. 14 along with the equivalent strength (Tsaï–Hill criterion) as defined by Grazide et al. (2018). The effect of curvature inversion observed on localized MoE obtained by FE modelling (Fig. 9) has been discarded by searching for the lowest positive localized MoE. Moreover, it can be observed visible on Fig. 9 and 13, where $x < 1100$ mm or $x > 1600$ mm that there is a local decrease of the localized MoE: this is due to the transversal compression induced by the loads q which models the pressure applied by loading heads (see Fig. 6). This effect has also been discarded by searching the minimum value only in the central part of 3 times the depth of the beam (which is x between 1137 mm and 1572 mm in this case).

Both in axial and bending loading, the general aspect of the minimum localized MoEs presented in Fig. 14 is similar to that of the local MoE (Fig. 10), even for the smallest sliding window length. For most of the tested y_k knot positions, the minimum localized MoEs obtained with BT and FE modelling were significantly different, which would certainly induce very different strength predictions in practice, as it was the case for the local MoE.

Under axial loading (Fig. 14 a,c,e), the main difference between the minimum localized MoEs relied on the difference between FE and BT modelling, but not significantly on the sliding window size.

In bending, as expected from the variations of localized MoE of Fig. 13, the localized MoE computed from the strains by FE modelling followed the evolutions of the minimum averaged MoE obtained by BT. Both were similar to the minimum apparent MoE obtained from BT when the sliding window size was 10 mm (Fig. 14 b), but they were more and more different as the sliding window size increased (Fig. 14 d,f).

Fig. 14 also shows that the Tsaï–Hill criteria had the same general aspect as the minimum localized MoEs. In bending in particular, Tsaï–Hill criterion variations were very similar to that of the minimum apparent MoE obtained from FE modelling, when the smallest sliding window length of 10 mm was used (Fig. 14 b). Under axial loading (Fig. 14 a), it was proportionally lower than the localized MoEs, being very low even when $y_k = -\frac{h}{4}$ (Tsaï–Hill criterion was divided by 2.8 relatively to material strength).

Based on the present study, it is not possible to determine which of these predictors would be better for strength prediction, however, it clearly shows that they behave differently in axial and bending loading, and according to knot position in the depth of the beam. The length of the sliding window across which these predictors were computed also had a significant influence, and the optimum sliding-window length should be searched, certainly depending on board cross-section as stated by Oscarsson et al. (2014).

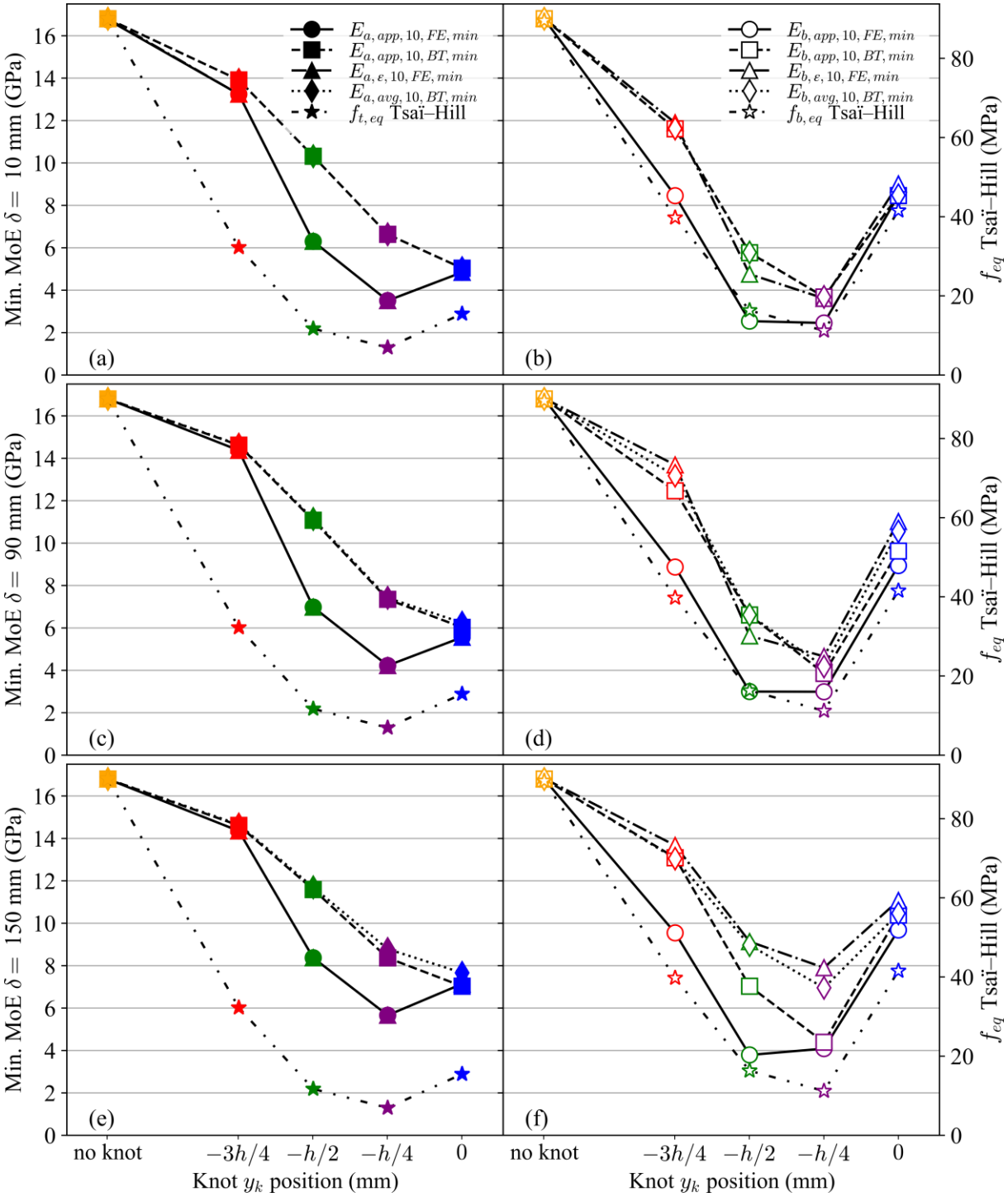

Fig. 14. Evolution of minimum localized MoEs and Tsaï-Hill criterion for axial loading (filled markers, on the left) and bending loading (empty markers, on the right) according to knot y_k position obtained by different modelling methods, with sliding windows lengths of 10 mm (a,b), 90 mm (c,d), and 150 mm (e,f). Tsaï–Hill criterion second axis scale has been set to be proportional to the apparent MoE for the homogeneous beam.

4. Conclusion

The models presented in this work mainly deal with artificial beams for which there is a relatively simple distribution of fibre orientation around knots: four different knot positions for a single diameter of knot were studied with in-plane fibre angle only. In reality, it is a 3D modelling problem and there is an immense diversity

in knot repartition and geometry. Keeping in mind these limitations, the results provided allow to draw some interesting conclusions, and the simplicity of the artificial beams can actually be seen as a way to highlight the typical behaviour of timber, modelling methods, and relative strength critera.

- The observation of beam deformations and the newly proposed computation of apparent MoE profiles from it showed that classical BT modelling, although taking into account the heterogeneity of local modulus in beam longitudinal direction, does not truly represent the actual deformations that can be depicted with FE modelling.
- In the considered tangential plane, axial and bending local MoEs, as defined in EN 408 (2012), of a given timber beam containing knots are generally different, and the relative difference depend on knot position. The axial local MoE is generally stiffer than bending local MoE (up to 30 % more), but it can be the other way around: it is 16 % more compliant in the case of a knot exactly centred in the middle line of the beam. This difference of stiffness according to loading type of timber containing knots is rarely discussed in the literature, whereas it may have consequences, *e.g.* in the strength grading of timber which can be performed on the basis of tensile or bending tests, and therefore lead to different results or yields.
- For beams modeled from artificial fibre angle data, the relative difference in local bending MoE predicted by FE and BT modelling can exceed 10 %, FE being stiffer for a centred knot, and more compliant for a knot close to beam edge. This stiffening effect is explained by the fact that when the knot is positioned close to the center of the beam, the fibers are optimally aligned with the principal stresses expected like in a uniform beam containing a void equivalent in diameter to the knot. Only FE modelling can account for this phenomenon.
- For modellings with fibre angle data coming from experimental LVL beams, local bending MoEs obtained from FE modelling were found to be more representative of the experimental data. and 6.3 % stiffer on average than that obtained from BT modelling. The high knottiness and possibly high proportion of fully embedded knots in the experimental LVL beams may justify this difference, following the previously mentioned stiffening effect in a beam when a knot is centred in this particular tangential plane.
- In bending, the different methods to compute localized MoEs behave differently according to knot position (thus fibre deviations within the beam) and to the sliding-window length across which they are computed, whereas it is less the case under axial loading for which it is mostly a matter of FE versus BT modelling method.
- The computation of localized bending MoE from the displacements proposed in the present paper, shortly called apparent MoE , exhibits a very different behaviour than the localized bending MoEs that currently exist in the literature. Indeed, the minimum bending apparent MoE along a beam containing knots behaves more similarly to the Tsaï-Hill strength criterion than the other studied minimum localized MoEs. The application and comparison of these strength predictors on the same experimental data are needed to conclude which one is better correlated to the actual bending strength.

Ultimately, this research highlights the intricate relationship between knot position, modeling approaches, and the resultant mechanical behaviours under different loading conditions. It highlights the need for refined modeling techniques that consider fiber deviations and emphasizes the challenges in predicting mechanical strength using localized MoE, particularly in bending scenarios. Further investigation is warranted to optimize sliding window lengths in relation with experimental results for accurate strength predictions based on localized MoE across varied board cross-sections.

5. Declarations

This study was funded by the region of Burgundy Franche-Comté and the French National Research Agency (EffiQuAss project ANR-21-CE10-0002-01).

The authors have no relevant financial or non-financial interests to disclose.

6. References

Baño V, Arriaga F, Soilán A, Guaita M (2011) Prediction of bending load capacity of timber beams using a finite element method simulation of knots and grain deviation. Biosyst Eng 109:241–249. https://doi.org/10.1016/j.biosystemseng.2011.05.008

Briggert A, Olsson A, Oscarsson J (2020) Prediction of tensile strength of sawn timber: definitions and performance of indicating properties based on surface laser scanning and dynamic excitation. Mater Struct 53:54. https://doi.org/10.1617/s11527-020-01460-5

Burger N, Glos P (1995) Relationship of moduli of elasticity in tension and in bending of solid timber. In: Proceedings of CIB-W18 Meeting. Copenhagen, Denmark, p Paper 28-5-2.

CEA (2018) Cast3M [Computer software], Finite element code developed by the CEA,(French atomic energy commission) https://www-cast3m.cea.fr/

Drewett TA (2015) The growth and quality of UK-grown Douglas-fir. Thèse, Edinburgh Napier University

Duriot R (2021) Développement de produits LVL de douglas aux propriétés mécaniques optimisées par l'exploitation de la mesure en ligne de l'orientation des fibres lors du déroulage. These de doctorat, HESAM

Duriot R, Pot G, Girardon S, Denaud L (2021a) New perspectives for LVL manufacturing wood of heterogeneous quality – Part. 2: Modeling and manufacturing of bending-optimized beams. Forests 12:1275. https://doi.org/10.3390/f12091275

Duriot R, Pot G, Girardon S, Roux B, Marcon B, Denaud L (2021b) New perspectives for LVL manufacturing wood of heterogeneous quality – Part. 1: Veneer mechanical grading based on online local wood fiber orientation measurement. Forests 12:1264. https://doi.org/10.3390/f12091264

Ehrhart T, Palma P, Schubert M, Steiger R, Frangi A (2022) Predicting the strength of European beech (Fagus sylvatica L.) boards using image-based local fibre direction data. Wood Sci Technol 56:123–146. https://doi.org/10.1007/s00226-021-01347-w

EN 338 (2016) Structural timber — Strength classes. CEN European Committee for Standardization, Brussels

EN 408 (2012) Timber structures – Structural timber and glued laminated timber – Determination of some physical and mechanical properties. CEN European Committee for Standardization, Brussels

Foley C (2001) A three-dimensional paradigm of fiber orientation in timber. Wood Sci Technol 35:453–465. https://doi.org/10.1007/s002260100112

Frayssinhes R, Girardon S, Denaud L, Collet R (2020) Modeling the Influence of Knots on Douglas-Fir Veneer Fiber Orientation. Fibers 8:54. https://doi.org/10.3390/fib8090054

Fuchs MB (2016). The Unit-Load Method. In: Structures and Their Analysis. Springer, Cham, pp 85–110. https://doi.org/10.1007/978-3-319-31081-7_6

Gil-Moreno D, Ridley-Ellis D, O'Ceallaigh C, Harte AM (2022) The relationship between bending and tension strength of Irish and UK spruce and pine. Eur J Wood Wood Prod 80:585–596. https://doi.org/10.1007/s00107-022-01787-6

Goodman JR, Bodig J (1980) Tension behavior of wood: an anisotropic, inhomogeneous material: final report to the National Science Foundation : grant ENG 76-84421. Colorado State University, Dept. of Civil Engineering, Fort Collins, Colorado

Grazide C, Coureau J-L, Cointe A, Morel S (2018) Mechanical performance curves for the strength grading of maritime pine. Eur J Wood Wood Prod 76:877–888. https://doi.org/10.1007/s00107-017-1241-4

Hanhijärvi A, Ranta-Maunus A (2008) Development of strength grading of timber using combined measurement techniques. Technical Report VTT Publications 686, VTT Technical Research Centre of Finland

Hankinson (1921) Investigation of crushing strength of spruce at varying angles of grain. Air Serv Inf Circ 3:16

Hu M, Olsson A, Hall S, Seifert T (2022) Fibre directions at a branch-stem junction in Norway spruce: a microscale investigation using X-ray computed tomography. Wood Sci Technol. https://doi.org/10.1007/s00226-021-01353-y

Hu M, Olsson A, Johansson M, Oscarsson J (2018) Modelling local bending stiffness based on fibre orientation in sawn timber. Eur J Wood Wood Prod 76:1605–1621. https://doi.org/10.1007/s00107-018-1348-2

Huber JAJ, Broman O, Ekevad M, Oja J, Hansson L (2022) A method for generating finite element models of wood boards from X-ray computed tomography scans. Comput Struct 260:106702. https://doi.org/10.1016/j.compstruc.2021.106702

Kretschmann DE (2010) Wood handbook, chapter 05: mechanical properties of wood. For. Prod. Lab. Dep. Agric. For. Serv. Madison Wis. USA

Longuetaud F, Pot G, Mothe F, Barthelemy A, Decelle R, Delconte F, Ge X, Guillaume G, Mancini T, Ravoajanahary T, Butaud J-C, Collet R, Debled-Rennesson I, Marcon B, Ngo P, Roux B, Viguier J (2022) Traceability and quality assessment of Douglas fir (Pseudotsuga menziesii (Mirb.) Franco) logs: the TreeTrace_Douglas database. Ann For Sci 79. https://doi.org/10.1186/s13595-022-01163-7

Lukacevic M, Kandler G, Hu M, Olsson A, Füssl J (2019) A 3D model for knots and related fiber deviations in sawn timber for prediction of mechanical properties of boards. Mater Des 166:107617. https://doi.org/10.1016/j.matdes.2019.107617

Nyström J (2003) Automatic measurement of fiber orientation in softwoods by using the tracheid effect. Computers and Electronics in Agriculture 41:91–99. https://doi.org/10.1016/S0168-1699(03)00045-0

Olsson A, Oscarsson J (2017) Strength grading on the basis of high resolution laser scanning and dynamic excitation: a full scale investigation of performance. Eur J Wood Wood Prod 75:17–31. https://doi.org/doi.org/10.1007/s00107-016-1102-6

Olsson A, Oscarsson J, Serrano E, Källsner B, Johansson M, Enquist B (2013) Prediction of timber bending strength and in-member cross-sectional stiffness variation on the basis of local wood fibre orientation. Eur J Wood Wood Prod 71:319–333. https://doi.org/10.1007/s00107-013-0684-5

Olsson A, Pot G, Viguier J, Faydi Y, Oscarsson J (2018) Performance of strength grading methods based on fibre orientation and axial resonance frequency applied to Norway spruce (Picea abies L.), Douglas fir (Pseudotsuga menziesii (Mirb.) Franco) and European oak (Quercus petraea (Matt.) Liebl./Quercus robur L.). Ann For Sci 75:102. https://doi.org/10.1007/s13595-018-0781-z

Olsson A, Pot G, Viguier J, Hu M, Oscarsson J (2022) Performance of timber board models for prediction of local bending stiffness and strength—with application on douglas fir sawn timber. WOOD FIBER Sci 54:226–245

Oscarsson J, Olsson A, Enquist B (2014) Localized Modulus of Elasticity in Timber and Its Significance for the Accuracy of Machine Strength Grading. Wood Fiber Sci 46:489–501

Pollet C, Henin J-M, Hébert J, Jourez B (2017) Effect of growth rate on the physical and mechanical properties of Douglas-fir in western Europe. Canadian Journal of Forest Research 47:1056–1065. https://doi.org/10.1139/cjfr-2016-0290

Rais A, Bacher M, Khaloian-Sarnaghi A, Zeilhofer M, Kovryga A, Fontanini F, Hilmers T, Westermayr M, Jacobs M, Pretzsch H, van de Kuilen J-W (2021) Local 3D fibre orientation for tensile strength prediction of European beech timber. Constr Build Mater 279:122527. https://doi.org/10.1016/j.conbuildmat.2021.122527

Saad K, Lengyel A (2022) Accurate finite element modelling of knots and related fibre deviations in structural timber. J King Saud Univ - Eng Sci. https://doi.org/10.1016/j.jksues.2022.01.005

Simonaho S-P, Tolonen Y, Rouvinen J, Silvennoinen R (2003) Laser light scattering from wood samples soaked in water or in benzyl benzoate. Optik-International Journal for Light and Electron Optics 114:445–448. https://doi.org/10.1078/0030-4026-00293

Steiger R, Arnold M (2009) Strength grading of Norway spruce structural timber: revisiting property relationships used in EN 338 classification system. Wood Sci Technol 43:259–278. https://doi.org/10.1007/s00226-008-0221-6

Viguier J (2015) Classement mécanique des bois de structure. Prise en compte des singularités dans la modélisation du comportement mécanique. [Strength grading of structural timber. Consideration of local singularities to predict mechanical properties]. PhD thesis, Université de Lorraine

Viguier J, Bourgeay C, Rohumaa A, Pot G, Denaud L (2018) An innovative method based on grain angle measurement to sort veneer and predict mechanical properties of beech laminated veneer lumber. Constr Build Mater 181:146–155. https://doi.org/10.1016/j.conbuildmat.2018.06.050

Viguier J, Bourreau D, Bocquet J-F, Pot G, Bléron L, Lanvin J-D (2017) Modelling mechanical properties of spruce and Douglas fir timber by means of X-ray and grain angle measurements for strength grading purpose. Eur J Wood Wood Prod 75:527–541. https://doi.org/10.1007/s00107-016-1149-4